A Chemical Odor Map in Cortex

A Chemical Odor Map in Cortex

A dissertation presented

By

Stanislav Pashkovski

to

The Division of Medical Sciences

in partial fulfillment of the requirements

for the degree of

Doctor of Philosophy

in the subject of

Neurobiology

Harvard University

Cambridge, Massachusetts

August 2017

A Chemical Odor Map in Cortex

Abstract

Odorous molecules trigger specific percepts. Appropriate assignment of odorants to corresponding percepts relies on the brain's ability to both discriminate distinct odorants, as well as generalize odorants that share chemical features. Although odorants evoke correlated activity across receptor expressing neurons in the olfactory epithelium and glomeruli residing in the olfactory bulb, it is unclear how the chemical attributes of odors are encoded in cortex to support both discrimination and generalization. To address this question, we have developed a preparation that allows us to monitor odor representations in awake mice across cortical layers in the main region of the brain devoted to olfactory processing, the Piriform Cortex (PCx). Using sets of odorants rationally designed to tile different regions of chemical odor space, we demonstrate that responses of neural ensembles in both Layer II (LII) and Layer III (LIII) of PCx preserve information about the physicochemical relationships between odor molecules in a manner conserved across individual mice. LII and LIII differ in terms of their correlation structure, reliability, odor sensitivity, and odor preferences, suggesting parallel representational strategies optimized for odor discrimination and generalization. These findings suggest that PCx harbors an invariant relational map of odorant space. The differential expression of this map across

distinct cortical layers further suggests complementary contributions to perception and odor-guided behavior.

TABLE OF CONTENTS

Dedications

Thank you to Bob for fostering such a sense of collective mission, for his unrelenting commitment and dedication, and for his continuous advocacy.

Thank you to Giuliano, Dan, Paul, Tari, Masha, and Alex for setting the bar.

Thank you to all the current and previous members of the lab that have made me never want to leave.

Most of all, thank you to my family for all of their support.

List of Figures

List of Tables

Chapter 1 Introduction

The mammalian olfactory system tightly couples odor detection with internal representations of past experience and immediate physiological demands to optimize a variety of behaviors necessary for survival.

In mice, odors bind distinct classes of olfactory sensory neurons (OSNs), defined by the expression of just 1 of 1000 different olfactory receptors (Axel, 2006). Each odor evokes a unique pattern of OSN activity that is relayed to higher-order olfactory areas via the olfactory bulb (OB) — the site of convergence for all OSNs-belonging to a unique class (Bozza, McGann, Mombaerts, & Wachowiak, 2004; Mombaerts, Wang, Dulac, Chao, & Nemes, 1996).

While OB projection neurons relay information to downstream targets from just one class of OSNs, this information diverges across several cortical and striatal olfactory areas such that each region may sample activity from all OSN classes (Igarashi & Mori, 2005; Miyamichi et al., 2010; Nagayama, Enerva, & Fletcher, 2010; Sosulski, Bloom, Cutforth, Axel, & Datta, 2012). Such connectivity enables unique interpretation and specialized processing of identical information that is integral for confluent execution of odor-guided behavior (Choi et al., 2011; Root, Denny, Hen, & Axel, 2014).

Perhaps the most studied target of the olfactory bulb is the Piriform Cortex. This area is a paleo-cortical structure thought to be involved in mediating higher-order olfactory functions such as odor discrimination, formation of unitary percepts from multi-component odors, and ultimately, odor-learning in a context and time appropriate manner (Chapuis & Wilson, 2011; Wilson & Sullivan, 2011; Wilson, Kadohisa, & Fletcher, 2006).

Essential to these higher order functions is the Piriform's capacity for representing an arbitrary number of odors and odor combinations (Wilson & Sullivan, 2011). These representations take the form of broadly distributed, sparse ensembles of neurons which display excitatory and inhibitory activity and evolve in time (Illig & Haberly, 2003; Rennaker, Chen, Ruyle, Sloan, & Wilson, 2007; Stettler & Axel, 2009).

Such response properties are thought to arise from the distributed structure of olfactory input from the OB as well as the interactions of recurrent feedforward excitation and local inhibition within the cortical network (Bekkers & Suzuki, 2013; Franks & Isaacson, 2006; Franks et al., 2011; Large, Vogler, Mielo, & Oswald, 2016; Poo & Isaacson, 2011; Suzuki & Bekkers, 2012).

Relating aspects of olfactory experience to features of this odor-evoked activity in PCx and understanding how such experience is encoded, transformed, and communicated to downstream targets to support perception and adaptive behavior are the main driving forces of current Piriform research.

Unfortunately, the field has been hampered in two ways. First, much of the characterization of PCx odor representations has been gathered with sparse sampling methods or under anesthesia (Barnes & Wilson, 2014b; 2014a; Courtiol & Wilson, 2014; M. Y. A. K. Mori, 2013; Narikiyo, Manabe, & Mori, 2014; Roland, Deneux, Franks, & Bathellier, 2017; Shanahan & Gottfried, 2014; Stettler & Axel, 2009; Tantirigama & Huang, 2017; Wilson, 2014; Wilson, Hoptman, Gerum, & Guilfoyle, 2011), conditions where cortical

processing is sufficiently different from that expected during wakefulness or ongoing behavior.

Secondly, the unpredictable nature of ligand-receptor interactions has made it difficult to define axes for grouping olfactory stimulii into comprehensive systematic arrangements that have proven so useful in vision and audition research. Researchers have relied primarily on artificially constrained odor arrangements that capture only a small fraction of the structural diversity of volatiles (Belluscio & Katz, 2001; Imamura, Mataga, & Mori, 1992; Rubin & Katz, 1999) or have not attempted to quantify odors at all.

More recently, a number of groups have begun to characterize volatiles using collections of metrics specifically designed to capture physicochemical molecular attributes that could ultimately influence binding interactions in the olfactory periphery (Haddad et al., 2008a; Haddad, Lapid, Harel, & Sobel, 2008b; Keller & Vosshall, 2016; Mainland et al., 2013; Mandairon, Poncelet, Bensafi, & Didier, 2009; Saito, Chi, Zhuang, Matsunami, & Mainland, 2009; Snitz et al., 2013). Collectively these studies confirm the utility of chemometrics for predicting olfactory-evoked activity at multiple stages of olfactory processing, and ultimately odor perception.

Here, we describe the development of a novel surgical preparation compatible with monitoring odor-evoked activity of cortical ensembles spanning both principal layers of PCx in awake mice. Using this approach, coupled with odor panels specifically chosen to tile multiple scales of odor space, we show that PCx represents odors according to their physicochemical similarity and that these representations are consistent across individuals.

LII and LIII use different strategies for representing odors. While odor encoding in LII is sparse and selective, deeper LIII appears to represent odors densely. These findings provide the first evidence for a chemical map of odors in PCx and challenge current models of PCx as a purely associative structure whose contribution to perception is thought to arise primarily via experience.

References

Axel, R. (2006). The Molecular Logic Of Smell. *Scientific American*, *16*(3s), 68–75. http://doi.org/10.1038/scientificamerican0906-68sp

Barnes, D. C., & Wilson, D. A. (2014a). Sleep and olfactory cortical plasticity. *Frontiers in Behavioral Neuroscience*, *8*, 2087. http://doi.org/10.3389/fnbeh.2014.00134

Barnes, D. C., & Wilson, D. A. (2014b). Slow-wave sleep-imposed replay modulates both strength and precision of memory. *The Journal of Neuroscience : the Official Journal of the Society for Neuroscience*, *34*(15), 5134–5142. http://doi.org/10.1523/JNEUROSCI.5274-13.2014

Bekkers, J. M., & Suzuki, N. (2013). Neurons and circuits for odor processing in the piriform cortex. *Trends in Neurosciences*, *36*(7), 429–438. http://doi.org/10.1016/j.tins.2013.04.005

Belluscio, L., & Katz, L. C. (2001). Symmetry, Stereotypy, and Topography of Odorant Representations in Mouse Olfactory Bulbs. *The Journal of Neuroscience*, *21*(6), 2113–2122. http://doi.org/10.1016/0165-0173(94)90007-8

Bozza, T., McGann, J. P., Mombaerts, P., & Wachowiak, M. (2004). In vivo imaging of neuronal activity by targeted expression of a genetically encoded probe in the mouse. *Neuron*, *42*(1), 9–21.

Chapuis, J., & Wilson, D. A. (2011). Bidirectional plasticity of cortical pattern recognition and behavioral sensory acuity. *Nature Publishing Group*, *15*(1), 155–161. http://doi.org/10.1038/nn.2966

Choi, G. B., Stettler, D. D., Kallman, B. R., Bhaskar, S. T., Fleischmann, A., & Axel, R. (2011). Driving Opposing Behaviors with Ensembles of Piriform Neurons. *Cell*, *146*(6), 1004–1015. http://doi.org/10.1016/j.cell.2011.07.041

Courtiol, E., & Wilson, D. A. (2014). Thalamic olfaction: characterizing odor processing in the mediodorsal thalamus of the rat. *Journal of Neurophysiology*, *111*(6), 1274–1285. http://doi.org/10.1152/jn.00741.2013

Franks, K. M., & Isaacson, J. S. (2006). Strong Single-Fiber Sensory Inputs to Olfactory Cortex: Implications for Olfactory Coding. *Neuron*, *49*(3), 357–363. http://doi.org/10.1016/j.neuron.2005.12.026

Franks, K. M., Russo, M. J., Sosulski, D. L., Mulligan, A. A., Siegelbaum, S. A., & Axel, R. (2011).

Recurrent Circuitry Dynamically Shapes the Activation of Piriform Cortex. *Neuron*, *72*(1), 49–56. http://doi.org/10.1016/j.neuron.2011.08.020

Haddad, R., Khan, R., Takahashi, Y. K., Mori, K., Harel, D., & Sobel, N. (2008a). A metric for odorant comparison. *Nature Methods*, *5*(5), 425–429. http://doi.org/10.1038/nmeth.1197

Haddad, R., Lapid, H., Harel, D., & Sobel, N. (2008b). Measuring smells. *Current Opinion in Neurobiology*, *18*(4), 438–444. http://doi.org/10.1016/j.conb.2008.09.007

Igarashi, K. M., & Mori, K. (2005). Spatial representation of hydrocarbon odorants in the ventrolateral zones of the rat olfactory bulb. *Journal of Neurophysiology*, *93*(2), 1007–1019. http://doi.org/10.1152/jn.00873.2004

Illig, K. R., & Haberly, L. B. (2003). Odor-evoked activity is spatially distributed in piriform cortex. *Journal of Comparative Neurology*, *457*(4), 361–373. http://doi.org/10.1002/cne.10557

Imamura, K., Mataga, N., & Mori, K. (1992). Coding of odor molecules by mitral/tufted cells in rabbit olfactory bulb. I. Aliphatic compounds. *Journal of Neurophysiology*.

Keller, A., & Vosshall, L. B. (2016). Olfactory perception of chemically diverse molecules. *BMC Neuroscience*, 1–17. http://doi.org/10.1186/s12868-016-0287-2

Large, A. M., Vogler, N. W., Mielo, S., & Oswald, A.-M. M. (2016). Balanced feedforward inhibition and dominant recurrent inhibition in olfactory cortex. *Proceedings of the National Academy of Sciences of the United States of America*, *113*(8), 2276–2281. http://doi.org/10.1073/pnas.1519295113

Mainland, J. D., Keller, A., Li, Y. R., Zhou, T., Trimmer, C., Snyder, L. L., et al. (2013). The missense of smell: functional variability in the human odorant receptor repertoire. *Nature Publishing Group*, *17*(1), 114–120. http://doi.org/10.1038/nn.3598

Mandairon, N., Poncelet, J., Bensafi, M., & Didier, A. (2009). Humans and Mice Express Similar Olfactory Preferences. *PloS One*, *4*(1), e4209. http://doi.org/10.1371/journal.pone.0004209

Miyamichi, K., Amat, F., Moussavi, F., Wang, C., Wickersham, I., Wall, N. R., et al. (2010). Cortical representations of olfactory input by trans-synaptic tracing. *Nature*. http://doi.org/doi:10.1038/nature09714

Mombaerts, P., Wang, F., Dulac, C., Chao, S., & Nemes, A. (1996). Visualizing an olfactory sensory map. *Cell*.

Mori, M. Y. A. K. (2013). Reorganization of neuronal circuits of the central olfactory system during postprandial sleep, 1–16. http://doi.org/10.3389/fncir.2013.00132/abstract

Nagayama, S., Enerva, A., & Fletcher, M. (2010). Differential Axonal Projection of Mitral and Tufted Cells in the Mouse Main Olfactory System. *Frontiers in Neural …*.

Narikiyo, K., Manabe, H., & Mori, K. (2014). Sharp wave-associated synchronized inputs from the piriform cortex activate olfactory tubercle neurons during slow-wave sleep. *Journal of Neurophysiology*, *111*(1), 72–81. http://doi.org/10.1152/jn.00535.2013

Poo, C., & Isaacson, J. S. (2011). A Major Role for Intracortical Circuits in the Strength and Tuning of Odor-Evoked Excitation in Olfactory Cortex. *Neuron*, *72*(1), 41–48. http://doi.org/10.1016/j.neuron.2011.08.015

Rennaker, R. L., Chen, C. F. F., Ruyle, A. M., Sloan, A. M., & Wilson, D. A. (2007). Spatial and Temporal Distribution of Odorant-Evoked Activity in the Piriform Cortex. *The Journal of Neuroscience*, *27*(7), 1534–1542. http://doi.org/10.1523/JNEUROSCI.4072-06.2007

Roland, B., Deneux, T., Franks, K. M., & Bathellier, B. (2017). Odor identity coding by distributed ensembles of neurons in the mouse olfactory cortex. *eLife*.

Root, C. M., Denny, C. A., Hen, R., & Axel, R. (2014). The participation of cortical amygdala in innate, odour-driven behaviour. *Nature*, *515*(7526), 269–273. http://doi.org/10.1038/nature13897

Rubin, B. D., & Katz, L. C. (1999). Optical imaging of odorant representations in the mammalian olfactory bulb. *Neuron*, *23*(3), 499–511.

Saito, H., Chi, Q., Zhuang, H., Matsunami, H., & Mainland, J. D. (2009). Odor Coding by a Mammalian Receptor Repertoire. *Science Signaling*, *2*(60), ra9–ra9. http://doi.org/10.1126/scisignal.2000016

Shanahan, L. K., & Gottfried, J. A. (2014). Olfactory Insights into Sleep-Dependent Learning and Memory. *Odor Memory and Perception* (1st ed., Vol. 208, pp. 309–343). Elsevier B.V. http://doi.org/10.1016/B978-0-444-63350-7.00012-7

Snitz, K., Yablonka, A., Weiss, T., Frumin, I., Khan, R. M., & Sobel, N. (2013). Predicting odor perceptual similarity from odor structure. *PLoS Computational Biology*, *9*(9), e1003184. http://doi.org/10.1371/journal.pcbi.1003184

Sosulski, D. L., Bloom, M. L., Cutforth, T., Axel, R., & Datta, S. R. (2012). Distinct representations of olfactory information in different cortical centres. *Nature*, *472*(7342), 213–216. http://doi.org/10.1038/nature09868

Stettler, D. D., & Axel, R. (2009). Representations of Odor in the Piriform Cortex. *Neuron*, *63*(6), 854–864. http://doi.org/10.1016/j.neuron.2009.09.005

Suzuki, N., & Bekkers, J. M. (2012). Microcircuits mediating feedforward and feedback synaptic inhibition in the piriform cortex. *Journal of Neuroscience*. http://doi.org/10.1523/JNEUROSCI.4112-11.2012

Tantirigama, M., & Huang, H. (2017). Spontaneous activity in the piriform cortex extends the dynamic range of cortical odor coding. Presented at the Proceedings of the …. http://doi.org/10.1073/pnas.1620939114

Wilson, D. A. (2014). Sleep and olfactory cortical plasticity, 1–11. http://doi.org/10.3389/fnbeh.2014.00134/abstract

Wilson, D. A., & Sullivan, R. M. (2011). Cortical Processing of Odor Objects. *Neuron*, *72*(4), 506–519. http://doi.org/10.1016/j.neuron.2011.10.027

Wilson, D. A., Hoptman, M. J., Gerum, S. V., & Guilfoyle, D. N. (2011). State-dependent functional connectivity of rat olfactory system assessed by fMRI. *Neuroscience Letters*, *497*(2), 69–73. http://doi.org/10.1016/j.neulet.2011.04.031

Wilson, D. A., Kadohisa, M., & Fletcher, M. L. (2006). Cortical contributions to olfaction: Plasticity and perception. *Seminars in Cell & Developmental Biology*, *17*(4), 462–470. http://doi.org/10.1016/j.semcdb.2006.04.008

Chapter 2 A Novel Preparation for Population Imaging of Piriform Cortex During Wakefulness

Introduction

In this chapter we describe the development of a novel experimental preparation that allows us for the first time to monitor odor-evoked activity in PCx ensembles during wakefulness. Using this new approach, we find that unlike under anesthesia, baseline activity of olfactory cortex in awake mice is substantially elevated and decorrelated. We show that during wakefulness, temporal dynamics of odor-evoked activity are substantially enriched, and neurons' response profiles are considerably reconfigured.

Methods

Surgical Approach

Prior to exposing PCx, mice are anesthetized with Isoflurane and head-fixed with dental cement to a rotating headpost. The surgical procedure involves resection of most of the musculature associated with the temporal aspect of the skull, and proceeds in several stages.

First, the skin overlying the temporal and mandibular muscles, is cut away from the whiskers rostrally, to the auditory meatus caudally. After cauterizing the facial vein, which channels blood from the orbital sinus to the jugular vein is cauterized, the superficial aspect of the zygomatic bone is exposed. The dorsal-posterior portion of the temporal muscle overlying the zygomatic bone is resected from the skull. To expose the ventral portion of the zygomatic bone, the mandibular muscle and associated fascia is resected along its entire rostro-caudal axis. This both, exposes the anterior tendon connecting this

muscle to the portion of the skull overlying the maxilla, as well as the articular surface of the jaw at the posterior portion of the mandible. The tendon is then severed and the zygomatic bone is isolated at both anterior and posterior junctions using a microdrill.

At this point, the mandible is only connected to the orbital muscular complex anteriorly, and to the retroglenoid vein at the articular surface. This vein serves as the venous drain from the entire ventral aspect of the brain and joins the mandibular and deep facial veins on its way to the jugular vein. At this point, the mandible must be further recessed ventrally in order to provide unhindered access to the optical objectives used in our imaging approach. However, disruption of any of these vessels is catastrophic. The cartilage connecting the articular surface of the mandible to the retroglenoid vein is transected along with associated musculature affixing the mandible to the external pterygoid process on the ventral portion of the skull. Rostrally, the mandible's coronoid process is disconnected from the tendons and orbital muscles connecting it to the eye. Finally, two strings are affixed to the articular surface and coronoid process on one end and attached to two screws affixed to the surgical baseplate on the other. The arrangement of the strings allows us to pull the mandible and associated musculature ventrally, while providing sufficient degrees of freedom for the subsequent portions of the surgery. At this point, the entire temporal aspect of the skull is exposed from the orbit, rostrally, to the junction of the squamosal bone and the external auditory meatus, caudally.

Finally, the fascia connecting the eye to the orbit is teased away from the skull surface to expose the orbital stalk. A small piece of Gelfoam soaked in saline containing

bovine thrombin is gently inserted into the orbit in order to apply pressure to the vasculature associated with the eye. The eye is immediately severed at the stalk and the orbit is further packed and pressurized with Gelfoam.

Hemifacial Analgesia

To ensure that the animal is free of pain and discomfort during wakefulness and semi-paralysis, we provide full hemifacial analgesia by performing a complete trigeminal nerve block. This procedure is designed to abolish sensation around our surgical exposure as well as the entire ipsilateral oro-facial region encompassing the entire dorsoventral extent of the head and extending from the nostril to the neck, rostrocaudally.

Access to the trigeminal ganglion is achieved as part of the full resection of the mandible. The junction of the four branches of the trigeminal ganglion, (the ophthalmic, infraorbital, maxillary, and mandibular nerve bundles) can be readily identified at the external pterygoid ridge.

To ensure that nerve-block lasts for the entire 3-4 hour imaging session, we inject a 1-5 ul, 0.2-1mg/kg dose of Bupivacaine directly into the stalk of the trigeminal nerve bundle using a calibrated micropipette mounted on a micro-manipulator. By infusing bupivacaine solution proximally to the trigeminal ganglion, distribution along all trigeminal branches, including the mandibular, ophthalmic, and infraorbital branches is guaranteed.

To ensure that block infiltrates the entire nerve bundle, each injection is supplemented with DiI, a contrast agent used to identify myelinated nerve fibers, due to its lipophilic, infiltrating nature (Maklad, Quinn, & Fritzsch, 2001). By including DiI in the block

solution and monitoring its diffusion through the nerve adjacent to the injection site, we are able to confirm proper micropipette placement directly inside the nerve bundle and not in nearby blood vessels. Successful DiI injection are characterized by uniform distribution of dye through the trigeminal bundle by proximal to the injection site. In cases of insufficient labelling of the nerve bundle, multiple injections are administered until the entire nerve is labelled by visual inspection. Despite delivering depolarization blockers close to the imaging site we have not noticed any injection associated decreases in spontaneous or odor-evoked activity of the Piriform network during imaging.

Evaluation of Hemifacial Analgesia

This procedure was initially evaluated and optimized in the following way. After bupivacaine injection, mice were allowed to recover in a restraint tube positioned on a heating blanket. Once righting reflex was regained, the spatial extent of peripheral nerve block was assessed by needle pricks along the entire dorsoverntral and rostrocaudal portion of the head ipsilateral to the injection site.

Heart rate and breathing rate was continually monitored for deviations that could indicate distress. Needle pricks were repeated every half an hour to determine the appropriate dose of Bupivicaine required to provide sufficiently long-lasting analgesia (3-4 hours).

Craniotomy

Imaging posterior PCx in awake mice is associated with substantial motor artifacts not typically encountered with imaging dorsal aspects of the brain. The site of our craniotomy—the squamosal bone—is almost free-floating. Caudally and ventrally, it is

bounded by the external auditory meatus and the tympanic bulla, respectively. Any animal motion during the imaging phase of the experiment results in axial movement of the brain that cannot be compensated by post-processing. In addition, the total area available for installing a cranial window is too small to permit the use of readily available cover-glass. During this portion of the surgery, we take several measures to create a stable, yet sufficiently large cranial window.

Instead of using thin glass coverslips, we cast thicker laminate windows from CYTOP, a fluorinated polymer. The biggest advantage of this polymer is that its index of refraction matches that of water, thereby reducing aberrations associated with glass cover-slipping. Furthermore, our laminate windows can be cut to any range of sizes between 0.5-3mm. Finally, the additional thickness of this coverslip allows sufficient depression of the brain surface to prevent axial movement during animal motion.

Given that imaging is performed almost immediately after installation of the cranial window, any pressure applied directly to the brain results in progressive buildup of cerebral spinal fluid between the dura and cortical surface. For this reason, the dura is gently teased away across the cranial opening prior to placement of the coverslip. The coverslip is then positioned and slightly depressed onto the brain surface using a micromanipulator.

Finally, a thick wall of dental cement is affixed around the coverslip covering any exposed portions of the skull and soft tissue. This further stabilizes the squamosal bone and largely abolishes any axial motion artifacts during imaging.

Semiparalysis

Unfortunately, stabilizing the craniotomy does not sufficiently eliminate motion artifacts encountered during imaging. As a result, we provide the animal with a continuous infusion of a low dose of the muscle relaxant Pancuronium Bromide during the imaging phase of the experiment.

The infusion line is placed into the jugular vein on the side contralateral to the exposure. The external jugular vein is first exposed at its junction with the acromiodeltoid and cephalic veins. The vein is then gently separated from the surrounding connective tissue, ligated, and partially transected (Asghar, 2002). A tip of an intravenous silicone catheter is then inserted through the pectoral muscle, dorsal to the clavicle, directly into the vascular lumen, and secured in place vetbond. The line is flushed with heparinized saline and hooked up to a variable-rate infusion pump. After calibration, the final dose and infusion speed was chosen to be 0.024 nanograms/kg/10 min. At this dose, mice experience a loss of righting reflex. Contraction of the diaphragm is not abolished, and toe-pinch reflex is maintained. Voluntary motion only occurs in response to noxious stimuli.

Blood pressure monitoring

During initial development of this procedure, heartrate and breathing rate monitoring were used to assess animal stability and effects of paralytic dosing. In addition, an arterial manometer placed directly into the femoral artery was used to monitor blood pressure.

Installation of the manometer occurred as follows. First, the superficial femoral

artery was exposed by making a 1cm incision along the inner thigh. Then, a 5-10 mm section of artery was carefully isolated and covered with a 2% lidocaine solution to prevent arterial constriction during cannulation. After placing two circular sutures around the exposed artery to prevent bleeding, the vessel was partially transected and a catheter (SciSense Inc.) was inserted with the tip oriented towards the heart and secured with two nylon sutures placed on either side of the insertion point. The two marginal sutures were then removed and the catheter flushed with heparinized saline before connecting the catheter to a manometer. Any deviations from normal values (between 300-600 bpm for heartrate and 80-160 mmHg for blood pressure) indicated either acute stress responses or paralytic overdosing; appropriate adjustments were made.

Fictive Sniffing

Mice rapidly adjust their sniff rate as part of active odor sampling and investigation (Verhagen, Wesson, Netoff, White, & Wachowiak, 2007; Welker, 1964), and changes in active sampling strongly influence neural representations of odors in olfactory bulb circuits (Carey & Wachowiak, 2011; Cury, 2010).

In order to control for potential differences in odor coding due to changes in odor sampling, we hijack the mouse's sniffing rhythm with a fixed computer controlled inspiration/expiration cycle synchronized in time to odor presentation. In so doing, we insure consistent odor delivery on with multiple exposures over the course of the experiment.

To do this, a cannula is placed into the nasopharynx via the trachea and

subsequently hooked up to a solenoid valve which draws air bidirectionally across the nasal epithelium (Cheung & Carey, 2009; Moldestad, Karlsen, Molden, & Storm, 2009). To place the cannula, a 1cm longitudinal incision is made over the trachea, beginning at the lower jaw and ending at the sternum. The exposed lobes of the thyroid gland and sternohyoid muscles are gently retracted, thereby exposing the trachea. Custom-cut polyethylene tubing is then placed through a single incision made in between a pair of tracheal rings below the cricothyroid and gently inserted via the vocal chords into the nasopharynx. The tube is secured to the trachea with a pair of nylon sutures and doused with silicone elastomer for further stability. The distal portion of the tube is then coupled to a computer driven solenoid valve and a vacuum line providing 150 ms long pulses of suction at a flow rate of 100 ml/min.

Image Registration

First, movies are aligned using a feature-based approach that is robust to regional fluorescence intensity fluctuations over the course of the experiment. Frames from a given experiment are first smoothed and contrast-normalized with a spatial kernel twice the size of a typical neuron in the FOV.

All frames from a single experiment are then registered to a manually chosen target frame in a pairwise manner. Features are automatically identified on the target frame using Harris corner detection. For all subsequent frames, feature displacement relative to target is calculated using the Lucas-Kanade (Lucas & Kanade, 1981) method at multiple spatial scales to accommodate small as well as large motion in the field-of-view (FOV).

Corresponding features are then used to calculate the homography transform that can best explain the displacement between frame and target. Given a set of at least 4 coordinates residing in one plane, a homography transform remaps these to a corresponding set in a different plane. It thus extends affine transforms (translation, scaling, rotation, shearing, and stretching) from a single to multiple planes. We find that homography-based registration, is the simplest approach to sufficiently compensate for uni-directional as well as nonuniform, elastic deformation of the FOV on the scale encountered in a typical experiment.

Cell Segmentation

Cells from aligned movies are subsequently identified using a semi-automated approach. First, the centroids of cells in a time-series average projection are manually identified. Cell masks are subsequently generated using a combination of morphological filtering and region-growing. To prevent signal cross-contamination from adjacent cells, each cell mask is further refined based on co-fluctuations in the pixel intensity in the cell's vicinity. Independently covarying groups of pixels are first identified using Nonnegative Matrix Factorization. Groups of pixels associated with the cell of interest are then assigned to the current mask. Those that correspond to adjacent neurons are excluded.

Finally, fluorescence time-courses for identified cells are obtained by averaging all pixels within corresponding masks on a frame-by frame basis across the experiment. Image registration, cell segmentation, and trace extraction is accomplished via custom scripts generated in-house that rely on publicly available Python image processing and

OpenCV packages. For image registration, functions for Harris corner detection, Lucas-Kanade based feature tracking, and homography transformation are publicly available as part of the “Feature Detection," "Object Tracking,” and "Camera Calibration and 3D Reconstruction” modules of OpenCV (Bradski, 2000) respectively. Cell segmentation and trace extraction scripts are publicly available at https://github.com/dattalab/d_code. Functions for morphological filtering and cell mask refinement are available as part of the Scikit-image (van der Walt et al., 2014) and Scikit-learn Python modules (Pedregosa et al., 2011).

Results

In order to obtain a head-to-head comparison of odor-evoked activity between wakefulness and anesthesia from the same neural population, we performed a 2-phase experiment. PCx of mice previously infected with the slow variant of Gcamp6, was acutely exposed. During both phases of the experiment mice were presented with 8 different monomolecular odors in a randomized manner for 2 seconds, with a 30-second inter-stimulus interval. Each odor was presented 10-15 times. At the end of Phase I, during which mice were awake, semi-paralyzed, and equipped with our fictive sniffing apparatus, anesthesia was delivered. Phase II proceeded immediately after. The use of the artificial sniffing apparatus eliminated any brain-state associated changes in respiration patterns that could influence odor encoding.

Assessing State Using Electroencephalography

Anesthesia is thought to induce a brain-state similar to slow wave sleep that is characterized by large-amplitude fluctuations in the 0.5 - 4 hz range and the absence of high-frequency activity from 30-60 hz that is typically present during wakefulness or behavioral engagement. Because power in the slow and fast frequency bands of the EEG is anti-correlated across these brain-states, their ratio has been traditionally used to assign an absolute value to the arousal state of the animal.

We recorded EEG activity across PCx and contralateral cerebellum to compare differences in brain state across the experiment. As shown in **Figure 2.1,** depicting overlaid trials acquired from both awake and anesthetized portions of the experiment, gamma power was substantially elevated during wakefulness, while delta power was only high under anesthesia.

For all 4 animals in this experiment the ratio of slow to fast wave power was used to set thresholds for acceptable levels for arousal for each experimental condition.

Spontaneous Activity is Elevated During Wakefulness

Spontaneous activity in cortical circuits has been shown to be highly susceptible to fluctuations in brain state (Haider et al., 2012). We therefore compared the character of baseline activity across cortical ensembles recorded under both anesthetized and awake conditions.

Unlike under anesthesia, during wakefulness a larger fraction of piriform neurons exhibited spontaneous activity (**Figure 2.2 A**). Overall, the frequency of spontaneous

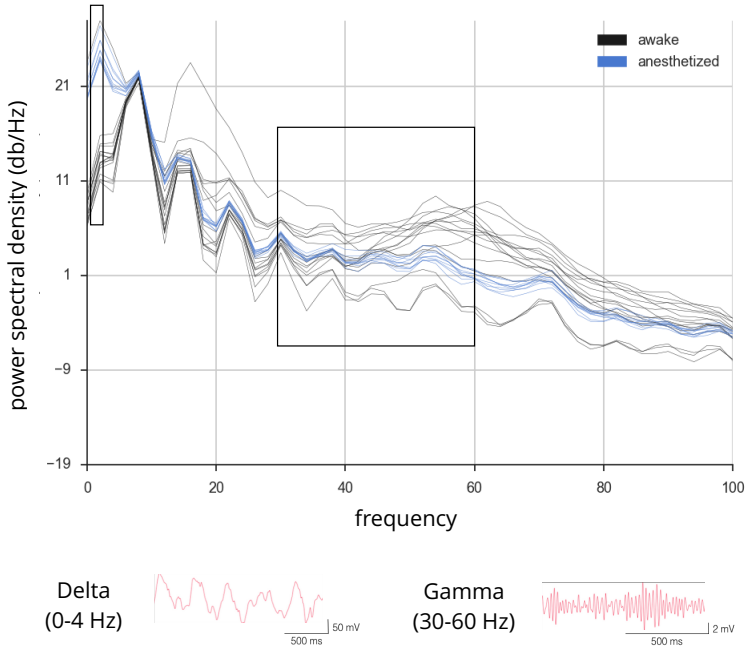

Figure 2.1 EEG-based Assessment of Brain State

Spectrogram from a single experiment depicting differences in slow and fast-wave activity across the experiment. Both Phase I (awake) and Phase II (anesthetized) are superimposed. Each trace corresponds to a 4-minute trial. The black rectangles indicate regions in the spectrum corresponding to the Delta and Gamma ranges (insets) of oscillatory activity. Note the reciprocal relationship between spectral density for each band across states.

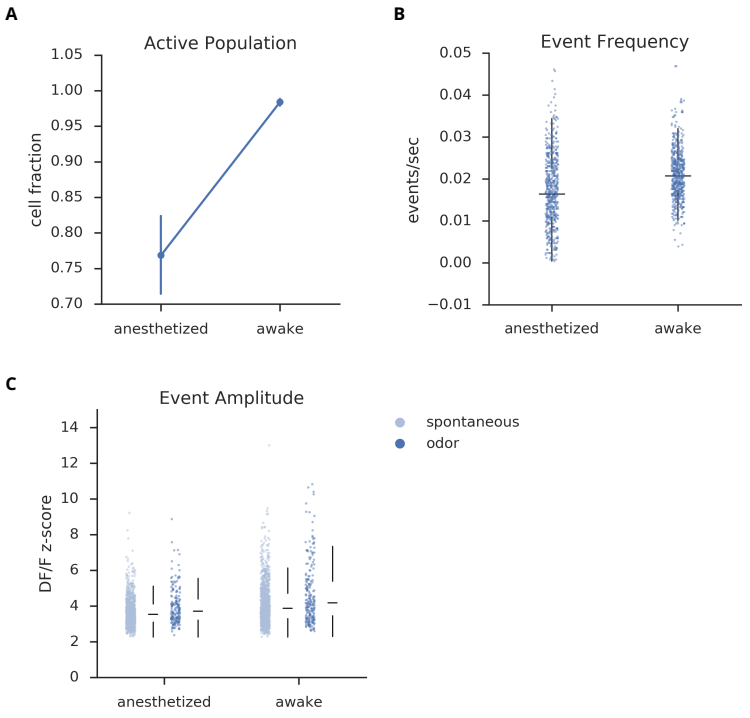

Figure 2.2 Anesthesia Attenuates Baseline Activity in PCx.

A. Change in fraction of active neurons across states defined by the presence of any spontaneous activity.

B. Distributions of event rates as a function of state. Note the overall reduction in spontaneous activity under anesthesia.

C. Distributions of standardized event amplitudes during baseline activity (inter-stimulus-interval) and odor presentation.

fluctuations in fluorescence across the populations increased. Although not significantly different, the amplitude of spontaneous “events” as well as event amplitudes associated with odor presentation, were elevated during wakefulness (**Figure 2.2 B,C**).

Enriched Temporal Dynamics During Wakefulness

There’s considerable evidence that temporal coding plays an especially important role in olfactory processing (Carleton, Bathellier, & Gschwend, 2010). The increase in spontaneous activity observed during wakefulness indicates an increase in the dynamic range of network activity (Tantirigama & Huang, 2017). This suggests that temporal dynamics of odor-evoked activity could also be increased during wakefulness. We therefore measured latency to response across both anesthetized and awake states as a simple proxy for the temporal evolution of odor-evoked activity.

While in the anesthetized state, responses tended to concentrate early in the response period, during wakefulness, responses tiled the odor period and extended well past odor offset (**Figure 2.3**). These results suggest that our awake preparation provides a suitable platform for characterizing cortical odor representations under conditions relevant for higher-order olfactory function.

Anesthesia Reconfigures Odor Tuning Profiles

State-dependent changes in neuromodulatory and inhibitory tone are intimately related to the selectivity of cortical activity at the single cell and population levels (Constantinople & Bruno, 2011; Fu et al., 2014; Haider et al., 2012). We therefore asked how response preferences of individual neurons changed as a function of anesthesia.

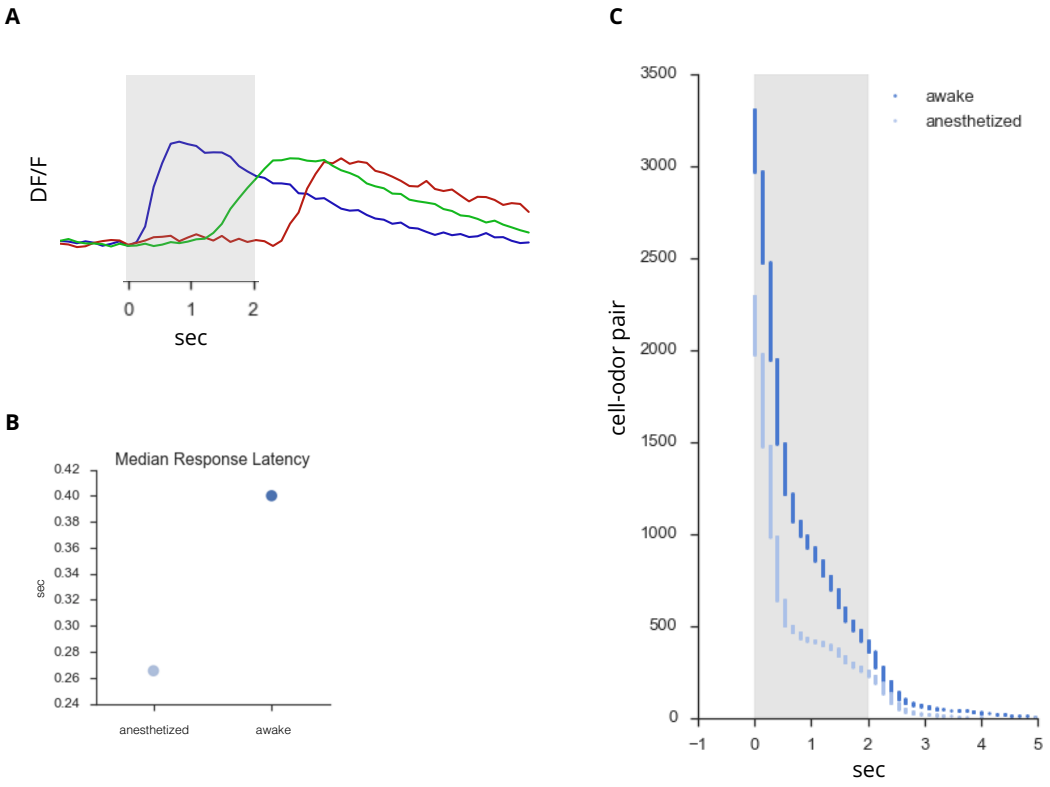

Figure 2.3 Anesthesia Reduces Odor-Evoked Dynamics

A. Single-trial responses from three different cells demonstrating typical response latencies observed during wakefulness. Grey bar indicates odor presentation period.

B. Median response latencies by state.

C. Sorted distributions of all odor-evoked responses presented by state. Note increase in responses occurring during the late portion of odor presentation as well as after odor offset.

Tuning profiles for single neurons were separately generated for the awake and anesthetized conditions. Neurons were then sorted using hierarchical clustering based on tuning similarity during wakefulness (**Figure 2.4 A top**). A substantial fraction of the population responded strongly and selectively to each odor in the panel. (**Figure 2.4 A bottom)** depicts tuning profiles for the same set of neurons from the anesthesia condition, with the same sorting order. Response profiles appear largely reconfigured. During wakefulness, neurons responded to slightly fewer odors on average (**Figure 2.4 B**) and tended to be more selective according to the lifetime sparseness measure.

These results indicate that odor-evoked activity in PCx is particularly sensitive to anesthesia associated changes in brain-state

Conclusions

Under physiologically normal conditions, state-dependent differences in network activity may reflect changes in functional connectivity between cortical and sub-cortical regions as well as preferential modulation of local excitatory or inhibitory circuit elements, and are likely indicative of behavior-appropriate circuit function (i.e. forraging, defensive behavior, rest, etc) (Fu et al., 2014). Studies of cortical sensory processing performed in anesthetized animals, on the other hand, provide only a marginal view of cortical function.

In this chapter, we show that baseline and odor-evoked activity in PCx differs substantially between anesthesia and wakefulness. Importantly, these finding validate the utility of the awake preparation for studying central odor representations.

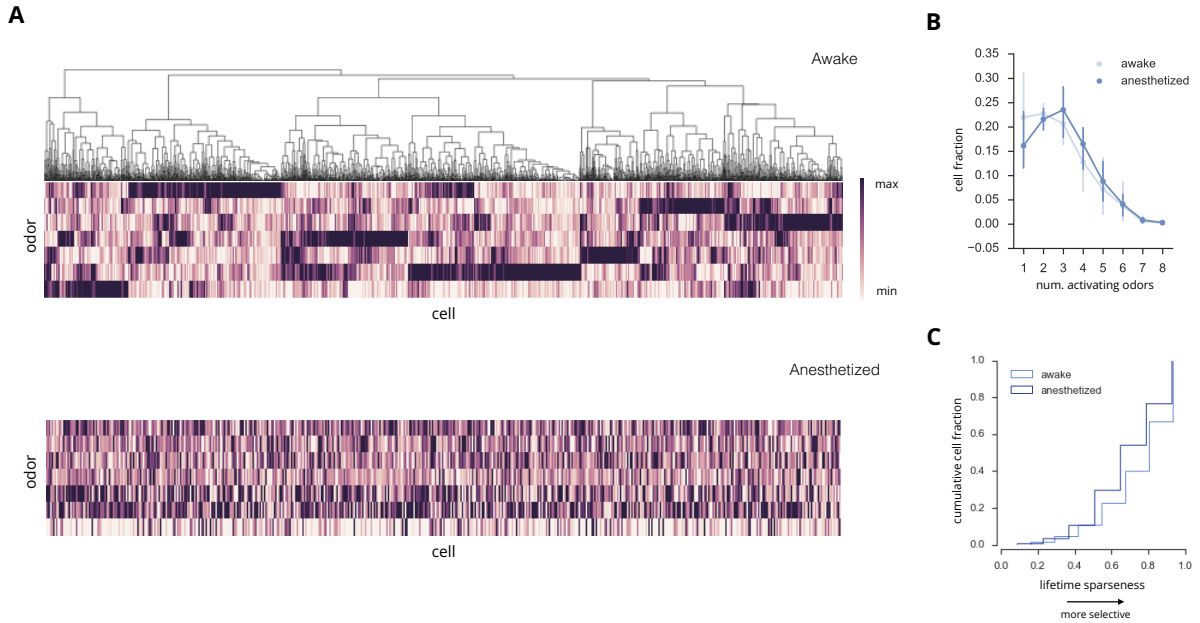

Figure 2.4 Response Profiles Are Reconfigured by Anesthesia

A. Top panel: hierarchically-clustered (complete linkage) trial-averaged responses (standardized dF/F) of all neurons in this experiment. Bottom panel: response profiles of the same neurons sorted according to clustering obtained in the awake state. Darker colors indicate stronger responses. Neuron tuning curves appear largely reconfigured between states.

B. Distribution of the fraction of neurons activated by 1 or more odor.

C. Cumulative probability distribution of lifetime sparseness values.

References

Asghar, M. (2002). external jugular catheter, 1–4.

Averbeck, B. B., Latham, P. E., & Pouget, A. (2006). Neural correlations, population coding and computation. *Nature Reviews Neuroscience*, *7*(5), 358–366. http://doi.org/10.1038/nrn1888

Bradski, G. (n.d.). Dr Dobb's Journal of Software Tools. 2000. *The OpenCV Library*.

Carey, R. M., & Wachowiak, M. (2011). Effect of Sniffing on the Temporal Structure of Mitral/Tufted Cell Output from the Olfactory Bulb. *The Journal of Neuroscience : the Official Journal of the Society for Neuroscience*, *31*(29), 10615–10626. http://doi.org/10.1523/JNEUROSCI.1805-11.2011

Carleton, A., Bathellier, B., & Gschwend, O. (2010). Temporal Coding in Olfaction, 329–352.

Cheung, M., & Carey, R. (2009). A Method for Generating Natural and User-Defined Sniffing Patterns in Anesthetized or Reduced Preparations. *Chemical Senses*.

Constantinople, C. M., & Bruno, R. M. (2011). Effects and Mechanisms of Wakefulness on Local Cortical Networks. *Neuron*, *69*(6), 1061–1068. http://doi.org/10.1016/j.neuron.2011.02.040

Cury, K. (2010). Robust Odor Coding via Inhalation-Coupled Transient Activity in the Mammalian Olfactory Bulb. *Neuron*.

Fu, Y., Tucciarone, J. M., Espinosa, J. S., Sheng, N., Darcy, D. P., Nicoll, R. A., et al. (2014). A cortical circuit for gain control by behavioral state. *Cell*, *156*(6), 1139–1152. http://doi.org/10.1016/j.cell.2014.01.050

Haider, B., Häusser, M., & Carandini, M. (2012). Inhibition dominates sensory responses in the awake cortex. *Nature*, *493*(7430), 1–6. http://doi.org/10.1038/nature11665

Harris, C., & Stephens, M. (1988). A combined corner and edge detector. *Alvey Vision Conference*.

Lucas, B. D., & Kanade, T. (1981). An iterative image registration technique with an application to stereo vision.

Maklad, A., Quinn, T., & Fritzsch, B. (2001). Intracranial distribution of the sympathetic system in mice: DiI tracing and immunocytochemical labeling. *The Anatomical Record*.

http://doi.org/10.1002/ar.1083

Moldestad, O., Karlsen, P., Molden, S., & Storm, J. F. (2009). Tracheotomy improves experiment success rate in mice during urethane anesthesia and stereotaxic surgery. *Journal of Neuroscience Methods*, *176*(2), 57–62. http://doi.org/10.1016/j.jneumeth.2008.08.015

Pedregosa, F., Varoquaux, G., Gramfort, A., Michel, V., Thirion, B., Grisel, O., et al. (2011). Scikit-learn: Machine Learning in Python. *Journal of Machine Learning Research*, *12*(Oct), 2825–2830.

Roland, B., Deneux, T., Franks, K. M., & Bathellier, B. (2017). Odor identity coding by distributed ensembles of neurons in the mouse olfactory cortex. *eLife*.

Stettler, D. D., & Axel, R. (2009). Representations of Odor in the Piriform Cortex. *Neuron*, *63*(6), 854–864. http://doi.org/10.1016/j.neuron.2009.09.005

Tantirigama, M., & Huang, H. (2017). Spontaneous activity in the piriform cortex extends the dynamic range of cortical odor coding. Presented at the Proceedings of the …. http://doi.org/10.1073/pnas.1620939114

van der Walt, S., Schönberger, J. L., Nunez-Iglesias, J., Boulogne, F., Warner, J. D., Yager, N., et al. (2014). scikit-image: image processing in Python. *PeerJ*, *2*(2), e453. http://doi.org/10.7717/peerj.453

Verhagen, J. V., Wesson, D. W., Netoff, T. I., White, J. A., & Wachowiak, M. (2007). Sniffing controls an adaptive filter of sensory input to the olfactory bulb. *Nature Neuroscience*, *10*(5), 631. http://doi.org/doi:10.1038/nn1892

Vinje, W. E., & Gallant, J. L. (2000). Sparse coding and decorrelation in primary visual cortex during natural vision. *Science*.

Welker, W. (1964). Analysis of sniffing of the albino rat. *Behaviour*.

Chapter 3 Mapping Odor Representations in Piriform Cortex

Introduction

To investigate the relationship between cortical odor representations and molecular structure, awake, head-fixed mice were exposed to odors during volumetric imaging of GcAMP6s expressing cortical ensembles residing in PCx layers II and III. Three experiments were performed with three different odor sets, systematically chosen to span molecular odor space at different scales.

Methods

Animal Methods

Acute imaging of Piriform cortex was performed in 8-16 week old C57/BL6J (Jackson Laboratories) male mice co-expressing the Vgat-ires-Cre transgene (Jackson Stock No. 028862) and Rosa-TdTomato (Jackson Stock No. 007914). TdTomato expression was limited to inhibitory neurons. This signal was used as a counter-stain for image alignment and registration. Male mice were group-housed prior to viral delivery and singly-housed for 1-3 weeks post-injection. All experiments were run in accordance with Harvard Medical School IACUC protocol number 04930.

Viral Delivery

Vgat-ires-Cre; Rosa-TdTomato male mice were injected with the slow version of the genetically encoded activity indicator GCaMP6: AAV1.CAG.GCaMP6s.WPRE.SV40 (Penn Vector Core). Using this Cre-independent viral strategy allows comprehensive labeling of both LII and LIII pyramidal neurons. Injections

were targeted to posterior Piriform cortex using Allen Brain Atlas coordinates: ML: -4.2, AP: -1.09, DV: -4.25, from the dura. 500-800 nl of full-titer virus was delivered at a rate of 10 nl every 10 seconds using a Nanoject II dispensing pump (Drummond Scientific). Imaging was performed 1-3 weeks after injection.

Surgical Methods

See Chapter 2 Methods: Surgical Approach

Imaging Volume Acquisition

High-speed volume imaging was performed using a 16KHZ resonant galvo - regular galvo pair (Cambridge Technologies) housed in a custom-designed microscopy equipped with 2-inch optics. Axial acquisition was performed with a large working distance Nikon 16x objective (N16XLWD-PF, 0.8 NA, 3mm WD) mounted on a high-speed piezo actuator (nPoint 400). A Coherent Chameleon laser tuned to 930 nm delivered 50-120 mW of excitation power at the front end of the objective. Emitted Fluorescence was detected using Hamamatsu H10770PA-40 PMTs. We used Scanimage 2015b to coordinate hardware and acquire imaging data. Imaging volumes spanned 210um across Piriform LII and LIII. Volumes were split into 6 optical slices each spanning 35um of cortex. Volumes were positioned such that 2 slices resided in LII and 4 slices resided in LIII. Given the greater density of pyramidal neurons in LII relative to LIII this configuration allowed simultaneous acquisition of fluorescence from roughly equal numbers of neurons from each layer. For correctly assigning neurons to either layer II or layer III we typically discarded a single optical slice that spanned the boundary between layers.

Image Registration

Individual optical slices from each movie were first aligned using a feature-based approach that was robust to regional fluorescence intensity fluctuations over the course of the experiment. Frames from a given experiment were first smoothed and contrast-normalized with a spatial kernel twice the size of a typical neuron in the FOV. All frames from a single experiment were then registered to a manually chosen target frame in a pairwise manner. Features in the FOV were automatically identified on the target frame using Harris corner detection. For all subsequent frames, feature displacement relative to target is calculated using the Lucas-Kanade method at multiple spatial scales to accommodate small as well as large motion in the field-of-view (FOV). Corresponding features were then used to calculate the homography transform that best explained the displacement between frame and target. Given a set of at least 4 coordinates residing in one plane, a homography transform remaps these to a corresponding set in a different plane. It thus extends affine transforms (translation, scaling, rotation, shearing, and stretching) from a single to multiple planes. We found that homography-based registration, was the simplest approach to sufficiently compensate for uni-directional as well as nonuniform, elastic deformation of the FOV on the scale encountered in a typical experiment.

ROI Detection and Signal Extraction

Following image registration, neuron detection, segmentation, and extraction of fluorescence signal was performed using the Suite2p software (Pachitariu, Stringer,

Dipoppa, & Schröder, 2017). This package implements neuropil fluorescence correction and correctly detects fluorescence sources from spatially overlapping neurons. Following automated neuron detection, cell masks were manually curated to exclude masks corresponding to non-somatic signal or to correct oversegmented cells.

Odor Set Design

A major goal of this study was to rationally design odor sets such that we could flexibly control the extent of similarities and differences between odorants in each odor panel. To do this we took advantage of 2 databases. The first is a collection of 2584 molecules commonly used in the flavors and perfume industries (www.TheGoodScentsCompany.com). A large fraction of these molecules are odorous; they are <300 daltons in size and sufficiently hydrophilic and volatile to readily access to the aqueous environment of the nasal epithelium. This database contains structurally diverse molecules that vary in cyclicity, branching, constituent functional groups, and other parameters. The second database is a set of 2270 statistical metrics designed to capture different molecular physicochemical properties (Dragon). Using this descriptor database, each of 2584 molecules could be represented by a vector containing 2270 values, thereby constituting a relational odor space where the similarity between any two molecules (in terms of atomic configuration, polarizability, molecular weight, van Der Waals volume, etc.) could be readily expressed as Euclidean distance between them.

Using this model odor space, we selected 3 distinct odor sets to explore how similarities and differences between odorants are represented in Piriform cortical activity.

These are referred to as Universal, Global, and Local odor sets to reflect the scale at which they sample our model odor space. Each odor set consisted of 22 odorants. The Universal odor set contained structurally diverse molecules chosen by sampling odor space broadly and uniformly. The Global Odor set was designed to ask whether odorant relationships in chemical space are preserved in patterns of neural activity. This odor set consisted of 6 groups of 3-4 molecules such that each group was maximally separated from the rest while molecules belonging to any single group were highly similar. Finally, for the Local odor set, we chose a set of closely-related aliphatic molecules that systematically varied in 1 dimension (number of carbon atoms in the chain). This odor set allowed us to describe how PCx represents odors at the local scale.

Odor selection for the first 2 odor sets was performed with Monte Carlo sampling. The cost function for the Universal odor set was designed to maximize separation between all 22 odors. To obtain well separated groups of molecules for the Global odor set, we used the silhouette coefficient as the cost function.

Detection of Odor Responses During Single Odor Presentations

In order to determine how reliably individual neurons responded to multiple presentations of the same odorant, excitatory responses on individual trials were defined as positive fluorescence transients during the 2-second odor presentation period whose mean magnitude exceeded 2.5 standard deviations of the mean signal calculated during the 2-second time window immediately preceding odor presentation.

auROC-Based Detection of Odor Responsive

To identify neurons that significantly responded to multiple presentations of the same odorant, we computed the area-under-the-receiver-operator-curve (auROC) statistic for each cell-odor pair. The auROC metric represents the probability that a neuron's response, chosen at random from all presentations of the same odor, will be ranked higher than a randomly chosen sham response obtained using baseline activity. A value of 0.5 indicates no difference between a neuron's activity during baseline and odor presentation. A value of 1 indicates a perfectly distinguishable excitatory response, while a value of 0 indicates a perfectly distinguishable suppressed response. For a single neuron and all presentations of a single odorant, we provided the classifier with the mean fluorescence obtained from 2-second time windows immediately flanking odor onset. A null distribution of auROC values for each cell-odor pair was constructed by randomly permuting the identity of the odor and baseline periods on each presentation. This was repeated 1000 times. The actual auROC value was deemed significant if it resided outside the 2.5-97.5th percentile of the null distribution. Neurons that did not display a significant response to any odors, according to auROC analysis, were excluded from all subsequent analysis.

Odor Sensitivity and Selectivity

Neurons vary in the degree to which they respond to odors in general as well as their preference for particular odors in the panel. We measured the tendency of a neuron to respond to multiple odors in the panel, a simple measure of tuning width, by simply counting the number of odors that yielded a significant positive auROC value.

To determine a neuron's odor-selectivity we computed the lifetime sparseness metric according to (Willmore & Tolhurst, 2001):

$$\text{lifetime sparseness} = \frac{1 - \left(\sum_j^N \frac{r_j}{N}\right)^2 / \left(\sum_j^N \frac{r_j^2}{N}\right)}{1 - \frac{1}{N}}$$

where r_j is the positive odor-evoked change in fluorescence to an odor j relative to baseline and averaged over multiple odor presentations, and N is the number of odors (22 in all odor sets). This value reflects the kurtosis of a neuron's tuning profile and ranges from 0 to 1. Highly peaked, narrow tuning profiles yield values close to 1 and represent neurons that respond strongly and selectively to few odors. Values close to 0 indicate equal responsiveness to a large fraction of the odor set.

Signal and ensemble correlation

The extent to which any two neurons have similar odor preferences can be assessed by computing the Pearson product moment correlation between their tuning curves. Repeating this for all neuron pairs provides a measure of overall similarity in odor preferences across a population of neurons. For each neuron, it's tuning curve was represented as a vector containing N elements, where N is the number of odors in the stimulus set. Each entry in this vector corresponds to the odor-evoked change in fluorescence relative to baseline and averaged over all presentations.

The same approach was used to measure shared odor preferences for neural ensembles. Here, we computed the Pearson product moment correlation between the

population responses to every pair of odors in our panel. For each odor, it's population response was represented as a vector containing N elements, where N is the number of neurons in the population. Each entry in this vector represents a single neuron's trial-averaged response to the corresponding odor. Populations were defined as all neurons belonging to either LII or LIII that responded to at least one odor according to the auROC analysis.

For this analysis, neural populations corresponding to each layer were pooled across multiple animals.

Mutual Information

Mutual information regarding odor identity or class was computed for individual neurons using normalized confusion matrices obtained from SVM classifiers. The following formula was used:

$$MI(x,y) = \sum_x \sum_y p(x,y) \cdot log_2 \frac{p(x,y)}{p(x) \cdot p(y)},$$

where x represents the actual odor/class and y represents the predicted odor/class. p(x) and p(y) refer to the marginal probabilities and p(x,y) is the joint probability obtained from the normalized confusion matrix.

Statistical Testing

For comparing two independent distributions when normality cannot be assumed Mann-Whitney U test was used. For comparing two paired samples when normality cannot be assumed we used Wilcoxon Signed Rank Test. For comparing two normal independent

distributions, Student's t-test was used. For testing significance of a single statistic against null distributions obtained by permutation, the true value was deemed significant if it resided outside the 2.5-97.5th percentile of the null statistic distribution. Error bars refer to either standard error of the mean or 97.5 confidence interval of the mean as indicated. For some statistical comparisons, effect size is reported using Cohen's d. Values ranging from 0-0.2, 0.2-0.5, and 0.5-2 indicate small, medium, and large effect sizes, respectively (Cohen, 1992).

Results

Differences in odor response properties between PCx layer II and III

Differences in local and global connectivity between PCx LII and LIII as well as reported differences in laminar response properties at the single cell level suggest that these layers could use distinct strategies for odor encoding at the population level. To characterize odor evoked activity across cortical layers, 3 mice were exposed to a diverse, "Universal" set of 22 monomolecular odorants that were selected based on maximal dissimilarity and homogeneous distribution in physicochemical descriptor space (**Figure 3.1,** 54% variance explained by PC1 and PC2).

Imaging volumes were positioned to capture approximately equal proportions of both layers (**Figure 3.2 A**). Roughly 1/3 of the imaging volume resided in LII, with the remainder positioned in LIII. Odor-evoked fluorescence transients acquired from cells residing in both layers (**Figure 3.2 B**) were characteristic of the expected response types typically observed with electrophysiological methods. Responses differed in amplitude,

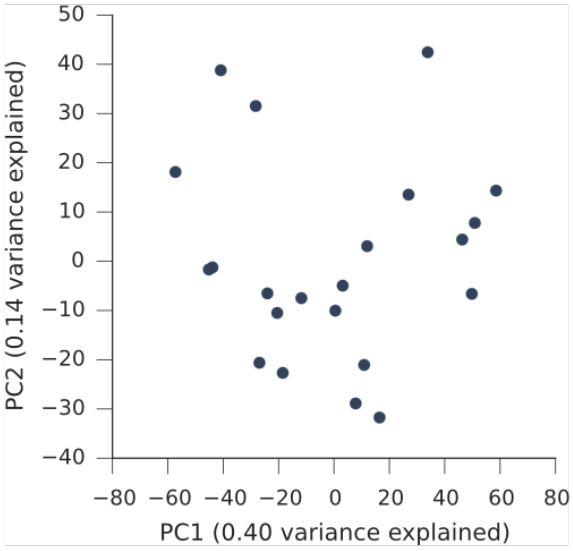

Figure 3.1 Universal Odor Set

Projection of 22 odors onto the first 2 principal components of chemical space. Odors were chosen based on maximal dispersion in the space defined by 2270 dimensions.

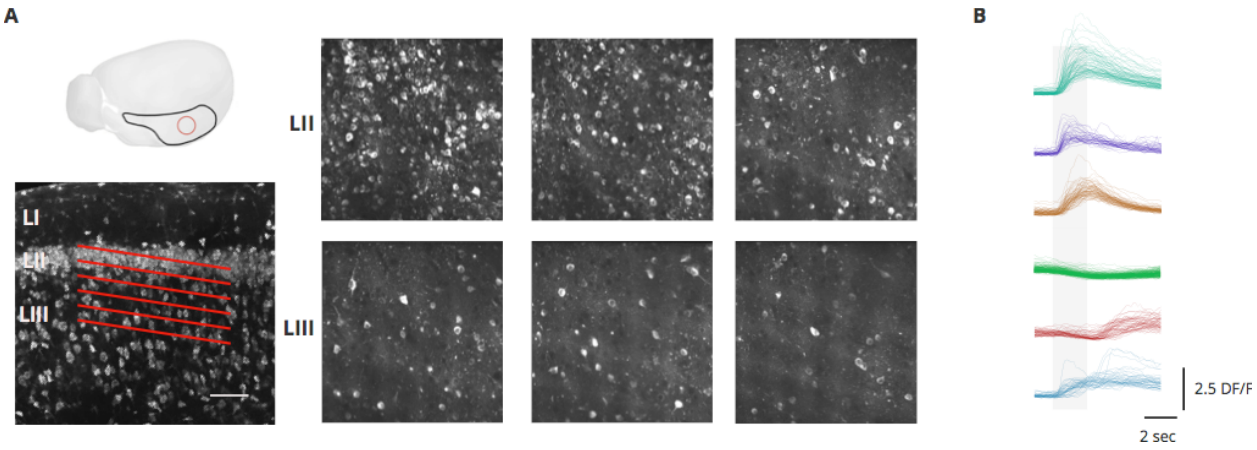

Figure 3.2 Volume Imaging of PCx LII and LIII

A. Top: Approximate position of craniotomy. **Bottom**: Coronal section of PCx with the position and orientation of each optical slice superimposed. Scale bar: 100 um. **Right**: Sample depiction of the fields of view corresponding to each optical slice in a typical imaging session. Top left FOV corresponds to the superficial optical slice from Layer II. Bottom right corresponds to the last optical slice from the left panel.

B. Trial-averaged fluorescence traces obtained from individual neurons across the volume clustered with a Gaussian mixture model. Response types differ in amplitude, latency to peak, and direction (excitation vs. suppression).

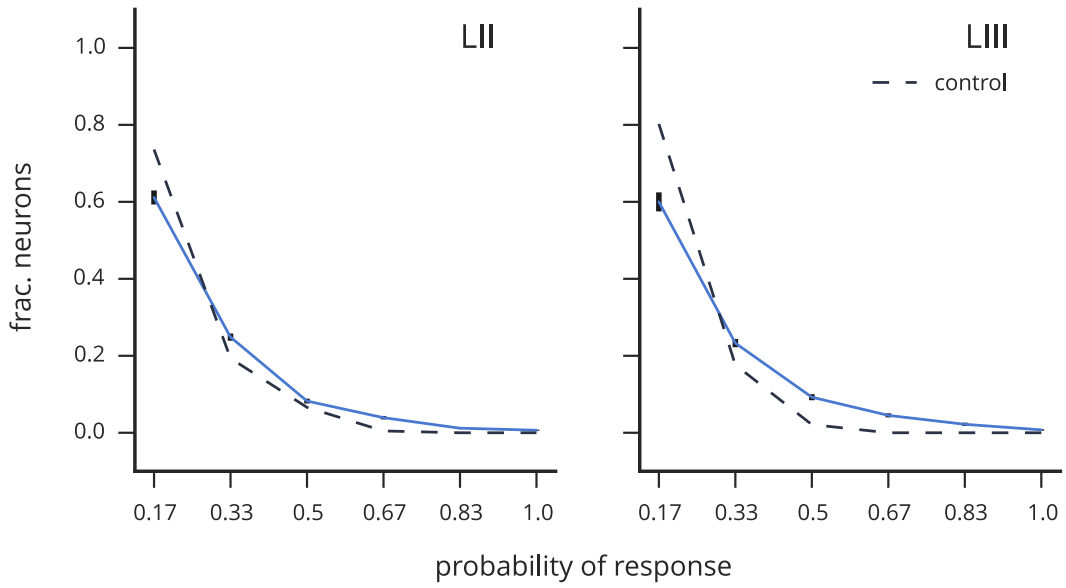

Figure 3.3 Greater Response Likelihood in LIII

Distribution of neuron response likelihood to multiple presentations of the same odor, presented as averages across different odors. Error bars indicate standard error from the mean. Responses were identified as odor-associated fluorescence signals that deviated more than 2.5 SD from the pre-odor baselines of the same length (2 sec). Stippled lines refer to fluorescent events identified in a period where no odor was delivered. In general, cortical neurons appear unreliable. Although there is a tendency for increased reliability in LIII, relative to baseline, neither LII nor LIII were significantly different from controls (Mann-Whitney U test; $p=0.24$, $p=0.15$, respectively). The distributions of response likelihood between layers were not significantly different (Mann-Whitney U test; $p=0.47$). For each layer, neurons were pooled across 2 animals.

directionality (suppression vs. excitation), and latency to peak. Odor onset as well as offset responses were common to both layers.

The likelihood of observing a response on multiple presentations of the same odor was modestly but not significantly greater for individual LIII neurons (**Figure 3.3**) (Mann-Whitney U test; p=0.47). Given the relatively low likelihood of response for most neurons, we defined reliable cell-odor pairs using an area-under-the-ROC curve classifier (Methods). A significant cell-odor pair was one whose auROC value for the distribution of response amplitudes corresponding to all presentations of a single odor was significantly different from a surrogate distribution obtained from activity in the time window immediately preceding odor presentation. Both LII and LIII harbored similar numbers of excitatory and suppressed responses (**Figure 3.4**, **A**) (Mann-Whitney U test; p=0.24, p=0.27, for excitatory and suppressed fractions respectively).

Despite the apparently low fraction of significant responses across the population more than 80% of neurons in both layers II and III responded to at least 1 odor in the panel (**Figure 3.4 B**). Of these cells, the size of the pool of neurons recruited by any given odor differed substantially by layer (**Figure 3.4 C**). On average, odors recruited activity in significantly more neurons in LIII than in LII: 30% vs. 11% (Wilcoxon Signed Rank Test; p<001).

Despite relatively similar sizes of the total responsive pools, this observation suggested that individual neurons in LIII were likely to be less selective. Indeed, LIII neurons

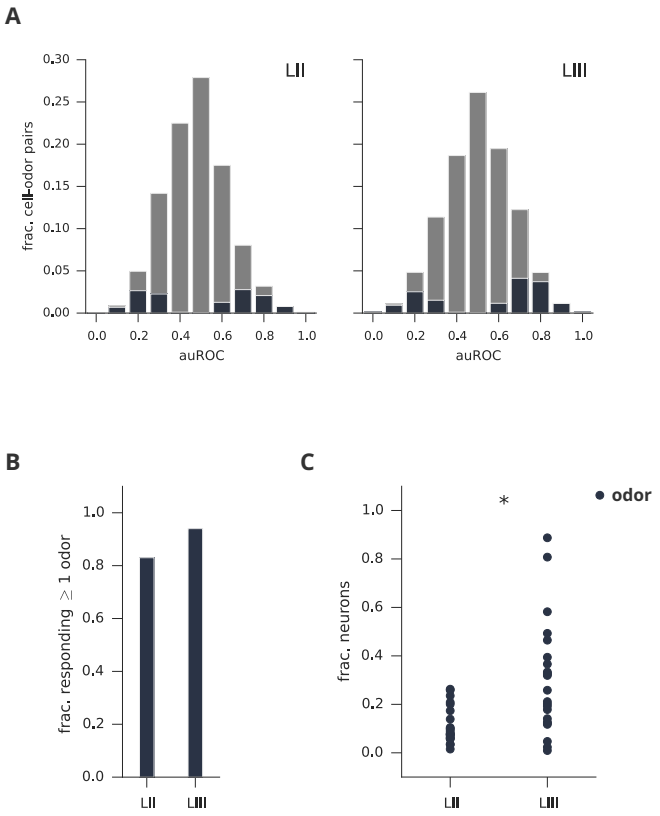

Figure 3.4 Larger odor-evoked ensembles in LIII

A. Distributions of excitatory and suppressed responses across layers. Dark grey bars indicate fractions of odor-cell response pairs deemed significant by auROC analysis. Values below 0.5 indicate suppression relative to pre-odor activity. Values above 0.5 represent excitatory responses. Despite a slight tendency for greater total excitatory responses in LIII, the differences in the fractions of suppressed or excitatory responses between LII and LIII were not significantly different (Mann-Whitney U test; p=0.24, p=0.27, for excitatory and suppressed fractions respectively). For each layer, neurons were pooled across 2 animals.

Figure 3.4 (Continued) Larger odor-evoked ensembles in LIII

B. Total responsive fraction of neurons. Most neurons in LII and LIII exhibit significant responses to at least 1 odor in the panel. Responsive neurons are identified using auROC analysis.

C. Size of odor-evoked ensembles. Collectively these neurons constitute the populations presented in **B.** On average, odors recruited activity in significantly more neurons in LIII than in LII: 30% vs. 11% (Wilcoxon Signed Rank Test; $p<001$).

appeared more promiscuous based on the larger number of odorants capable of eliciting a response from a single neuron (**Figure 3.5 A**). Most neurons in LII responded to 3 or fewer odors (83% in LII vs 70% in LIII). Neurons tended to respond to more odors in LIII. The distributions were not significantly different (Mann-Whitney U test; p=0.09). Similarly, relative to LII, lifetime sparseness values across the LIII population were skewed in favor of less selective (0 is least selective) (**Figure 3.5 B**) (Mann-Whitney U test; $p<0.001$).

Together, these results indicate that both PCx LII and LIII harbor moderately reliable neurons whose activity is bi-directionally modulated by odor presentation. At the population level, relative to LII, recruited LIII ensembles appear denser and consist of neurons with more broadly tuned response profiles. Furthermore, the sparse, moderately selective population responses characteristic of LII are consistent with coding strategies well-suited for decorrelating similar odors while the dense, less selective activity in LIII is consistent with compressed representation strategies that may be well suited for efficient generalization between similar odors.

Complementary Representations of Odor Similarity Across LII and LIII

Given the broadly-tuned, denser ensemble activity observed in LIII, we reasoned that deeper PCx could harbor a compressed representation of odor space. In this context, structurally similar odorants should remain decorrelated in superficial PCx but become consolidated by LIII ensembles.

To determine how similarity relationships are mapped in neural activity across LII and LIII, we designed a 22 monomolecular odor set organized into 6 groups defined by the

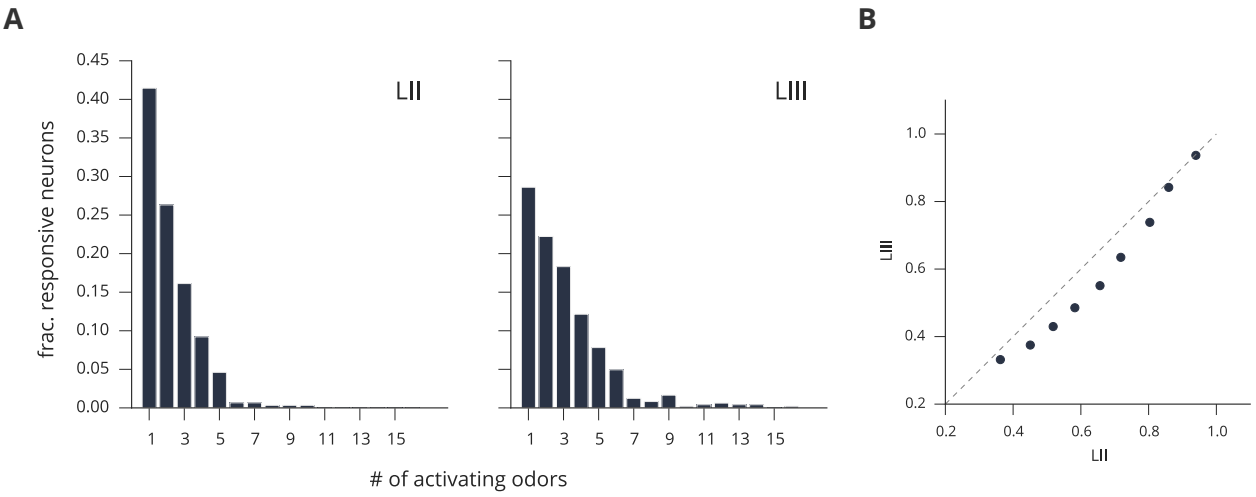

Figure 3.5 LIII Neurons Respond More Broadly

A. Distribution of neuron sensitivity to odor stimulation. Of 22 diverse odors in the Universal panel, most neurons in LII responded to 3 or fewer odors (83% vs 70% in LIII). Neurons tended to respond to more odors in LIII. The distributions were not significantly different (Mann-Whitney U test; $p=0.09$).

B. Decile-decile plot of lifetime sparseness distributions obtained from neurons belonging to LII and LIII. A Lifetime sparseness value of 1 indicates most selective; 0 indicates least selective. Collectively, LII neurons were significantly more selective than LIII neurons as indicated by distribution deciles below the unity line (Mann-Whitney U test; $p<0.001$).

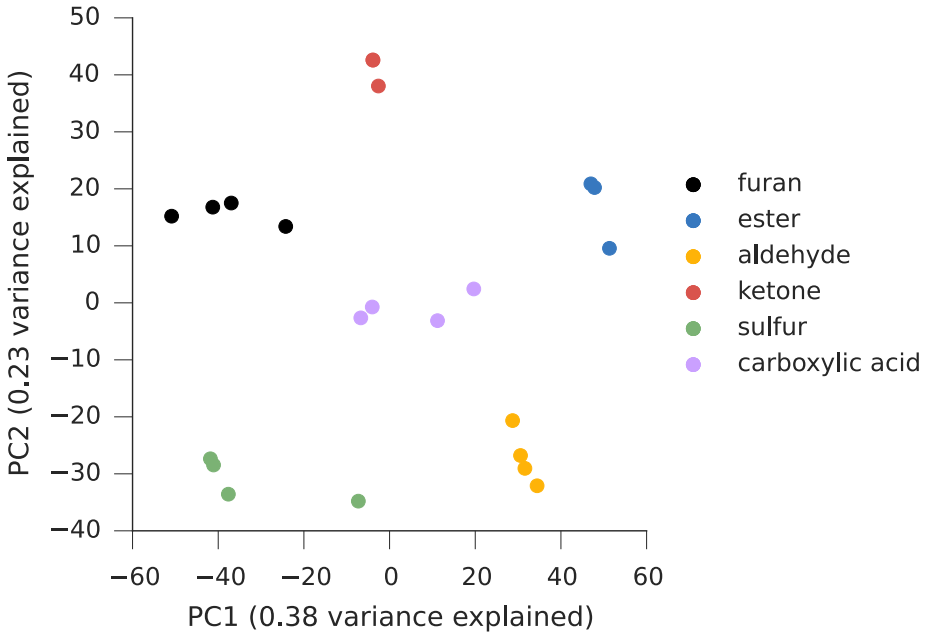

Figure 3.6 Global Odor Set

Projection of 22 odors onto the first 2 principal components of chemical space. Odors were chosen based on functional group as indicated in the legend. This odor set was designed such that the 6 groups were maximally dispersed in the 2270-dimensional odor space, while at the same time, minimizing distance between molecules belonging to a single group.

presence of a distinct functional moiety (**Figure 3.6**). Odors were chosen to maximize within-group similarity and maximize across-group distance in odor space (Methods); this panel will be referred to as the "Global" odor set to indicate the scale of separation between groups. Data in this experiment was gathered from 3 animals.

The increase in physicochemical similarity for this set relative to the Universal odor panel resulted in an increase in variance captured by the first 2 principal components from 54% to 61% (**Figure 3.6**). While the overall fraction of responsive neurons obtained for both Universal and Global odor sets was similar (**Figure 3.4 B, Figure 3.7 A**), LII and LIII neurons probed with the Global panel tended to be activated by more odors **(Figure 3.5 A, Figure 3.7 B**). For the Global odor panel, most neurons in LII responded to 4 or fewer odors (69% vs 45% in LIII). Neurons responded to significantly more odors in LIII (Mann-Whitney U test; $p<0.05$). Similarly, lifetime sparseness distributions for both layers were greater than those observed in the Universal experiment (**Figure 3.5 B, Figure 3.7 C**), although in this experiment, LIII response profiles appeared substantially broader relative to LII (Mann-Whitney U test; $p<0.001$).

Interestingly, while the overall size of evoked ensembles in layer II was comparable to that observed with the Universal odor set, LIII ensemble sizes were more uniform across the stimulus set **(Figure 3.7 D**). This could be circumstantially associated with the particular configuration of chosen molecules or could reflect the overall decrease in molecular diversity of this panel relative to the Universal odor set. For the Global panel, odors

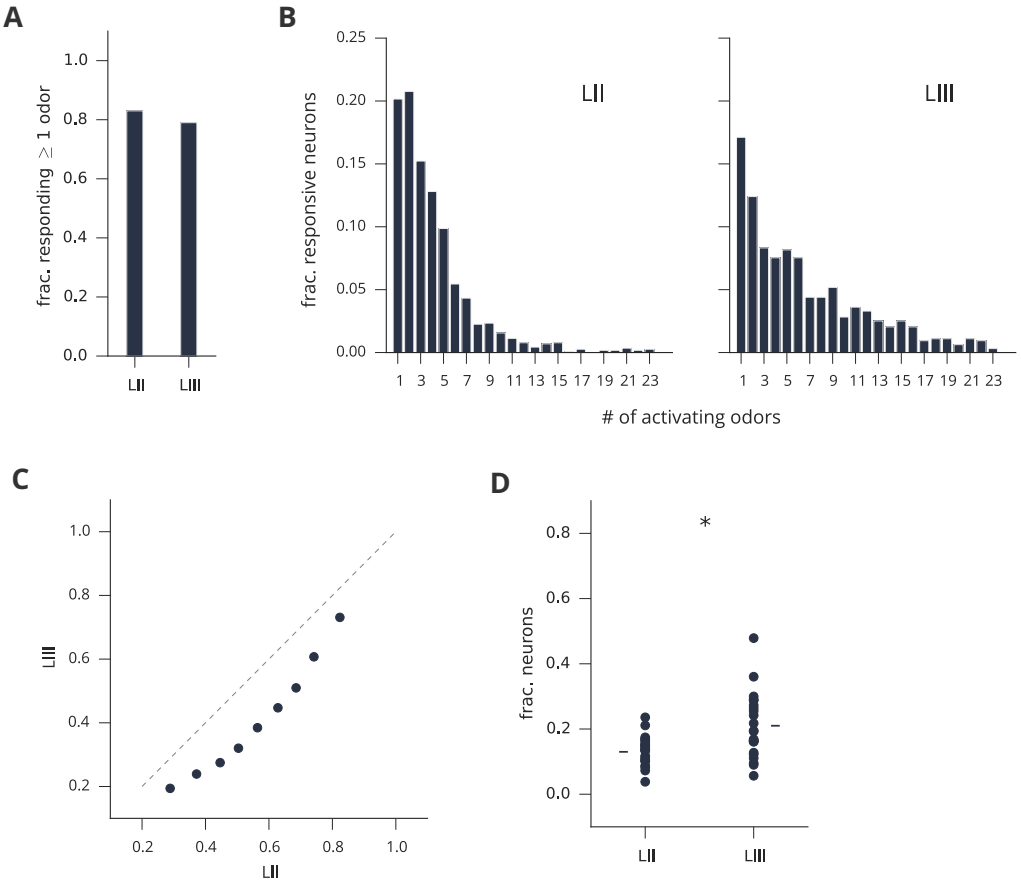

Figure 3.7 LII and LIII Response Profiles to Global Odor Set are Broader

A. Fraction of neurons responding to at least 1 odor.

B. Distribution of neuron sensitivity to odor stimulation. Of 22 odors in the Global panel, most neurons in LII responded to 4 or fewer odors (69% vs 45% in LIII). Neurons responded to significantly more odors in LIII (Mann-Whitney U test; $p<0.05$).

C Decile-decile plot of lifetime sparseness distributions obtained from neurons belonging to LII and LIII. A Lifetime sparseness value of 1 indicates most selective; 0 indicates least selective. Collectively, LII neurons were significantly more selective than LIII neurons (Mann-Whitney U test; $p<0.001$).

D. Size of odor-evoked ensembles. Collectively these neurons constitute the populations presented in **A.** On average, odors recruited activity in significantly more neurons in LIII than in LII: 21% vs. 13% respectively (Wilcoxon Signed Rank Test; $p<001$).

recruited activity in significantly more neurons in LIII than in LII: 21% vs. 13% (Wilcoxon Signed Rank Test; $p<001$).

Neural populations that discriminate efficiently typically consist of neurons with dissimilar tuning profiles (Averbeck, Latham, & Pouget, 2006; Vinje & Gallant, 2000). We therefore compared the distributions of both signal and ensemble correlations across LII and LIII. We defined signal correlations as the product moment correlation coefficient between 2 trial-averaged response vectors for any pair of neurons, where each entry in the vector corresponds to a single odor in the panel. Ensemble correlations provide a sense for the similarity of the population response: for a vector corresponding to each odor in the panel, a single entry refers to a neuron's trial-averaged response.

Distributions of pairwise signal correlations in LII and LIII were both significantly right-skewed relative to corresponding control distributions created by permuting stimulus order (LII actual mean = 0.02 vs. control mean = 0.0 and LIII actual mean = 0.09 vs control mean = 0.0; Student's t test; $p<0.001$). However, LIII harbored significantly more neuron pairs with similar response profiles indicating a greater overall response similarity at the population level (**Figure 3.8 A**) (LIII mean= 0.09±0.25 vs. LII mean = 0.02±0.23; Student's t test; $p<0.001$).

Shared odor preferences between individual neurons in LIII suggests that odor-evoked activity in deeper PCx should be distributed across groups of neurons that overlap to a greater extent than in LII. We therefore measured ensemble correlations independently in each layer (Methods) (**Figure 3.8 B**). On average, ensemble correlations

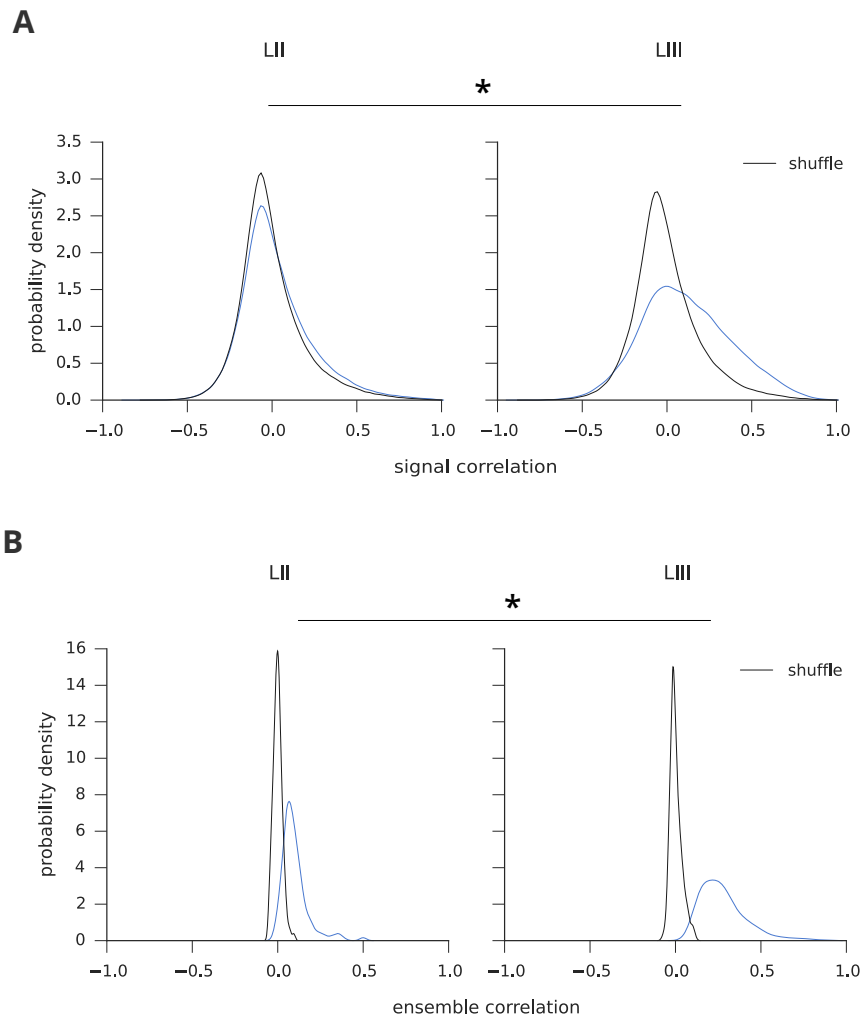

Figure 3.8 Stronger Correlation structure in LIII

A. Signal correlation distributions obtained from all pairs of neurons, presented by layer. Signal correlation is defined as the Pearson product moment correlation coefficient between two neurons' tuning curves. For each neuron, it's tuning curve was represented as a vector containing N elements, where N is the number of odors in the stimulus set. Each entry in this vector corresponds to the odor-evoked change in fluorescence relative to baseline and averaged over all presentations. Shuffled distributions were constructed

by independently permuting the order of each neuron's tuning curve vector. On average, signal correlations were higher in LIII relative to LII; LIII mean= 0.09±0.25 vs. LII mean = 0.02±0.23 (Student's t test; $p<0.001$). Signal correlations within each layer were also significantly higher than shuffled control distributions (LII actual mean = 0.02 vs. control mean = 0.0 and LIII actual mean = 0.09 vs control mean = 0.0; Student's t test; $p<0.001$). **B.** Distributions of ensemble correlations computed as in **A** but on population responses for each pair of odors. For each odor, it's population response was represented as a vector containing N elements, where N is the number of neurons in the population. Each entry in this vector represents a single neuron's trial-averaged response to the corresponding odor. Shuffled distributions are constructed by independently permuting the order of neurons in each odor's ensemble vector. Populations were defined as all neurons belonging to either LII or LIII that responded to at least one odor according to the auROC analysis. On average, ensemble correlations were higher in LIII relative to LII; LIII mean= 0.28±0.13 vs. LII mean = 0.1±0.08 (Student's t test; $p<0.001$). Ensemble correlations within each layer were also significantly higher than shuffled distributions (LII actual mean = 0.28 vs. control mean = 0.0 and LIII actual mean = 0.1 vs control mean = 0.0; Student's t test; $p<0.001$).

were higher in LIII relative to LII; LIII mean= 0.28±0.13 vs. LII mean = 0.1±0.08 (Student's t test; $p<0.001$). Ensemble correlations within each layer were also significantly higher than shuffled distributions (LII actual mean = 0.28 vs. control mean = 0.0 and LIII actual mean = 0.1 vs control mean = 0.0; Student's t test; $p<0.001$).

Consistent with increased odor sensitivity of LIII neurons, these results indicate that in deep PCx, odors activate shared pools of neurons that appear to behave non-selectively. Odor representations in LII on the other hand appear decorrelated.

Increased response similarity at the population level in deep PCx could result from increased similarity of representations within groups or from indiscriminate increases in similarity across the entire panel. To assess the similarity structure of ensemble representations across layers we constructed distance matrices from odor-ensemble responses. Each entry in these matrices is a measure of separation between any two odors expressed in terms of neural activity. We then embedded these relationships in a 2-dimensional subspace using metric multi-dimensional scaling (Methods). The same approach was used to embed the odor panel in physicochemical descriptor space.

Surprisingly, in both LII and LIII, separation between the 6 groups of odors was conserved (**Figure 3.9 B,C**). While within each group odors appeared scattered in LII, LIII exhibited greater concentration of group members **(Figure 3.9 C,D**) (Wilcoxon Signed Rank Test; $p<0.05$). The groups also appeared better separated from each other in LIII. This effect likely requires collective neural activity, as individual neurons did not display strong

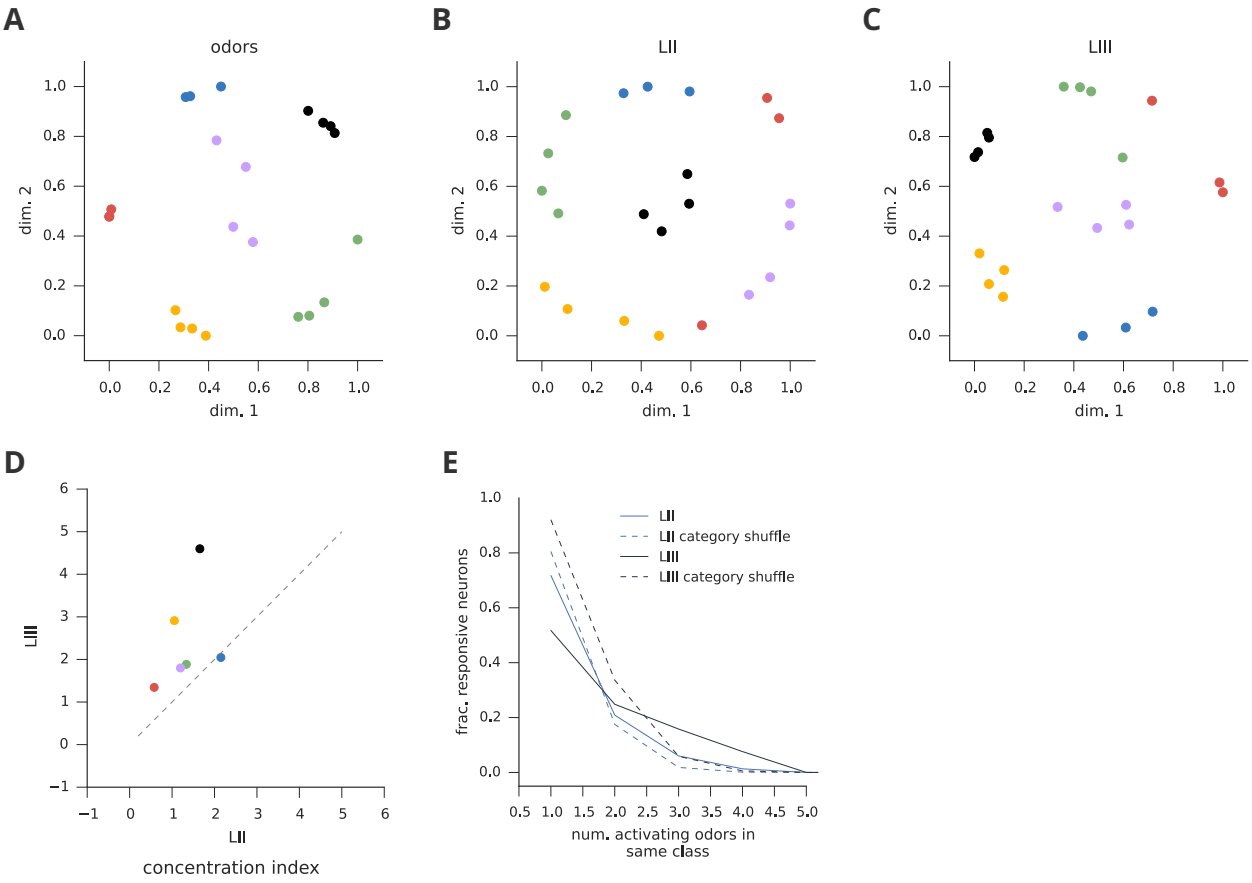

Figure 3.9 Enhanced Clustering of Similar Odors in LIII

Embedding of odors using metric multi-dimensional scaling (MDS) based on either physicochemical descriptor data or neural activity. For embedding neural activity, pseudopopulations were constructed by combining neurons belonging to either LII or LIII from 3 animals. For each embedding, 10 MDS runs were performed to insure stability and convergence of the algorithm. Each run was initialized with 500 random restarts.

A. MDS embedding of odors using physicochemical descriptors. Each odor was represented with a vector containing 2270 z-scored descriptor values. Pairwise distances between each pair of odor vectors were computed using normalized Euclidean distance

Figure 3.9 (Continued) Enhanced Clustering of Similar Odors in LIII

and supplied to the algorithm. Each dot represents an odor. Colors indicate different odor classes, as in Figure 3.6.

B. and **C.** MDS embedding of odors using population activity from either LII or LIII. For embedding neural activity we first created population response matrices (pooled by layer across 3 animals). Each row vector in this matrix corresponds to all neurons' trial-averaged responses to a single odor. The dimensionality of each matrix was reduced with PCA such that 50% of overall variance was captured in each layer (with 7 principal components in LII and with 5 principal components in LIII). Pairwise distances for each pair of transformed odor vectors were computed using normalized Euclidean distance and supplied to MDS. Odors in LIII appear to cluster according to functional group class. In LII odors within any single group appear better separated.

D. Depiction of cluster concentration by layer. For each functional class, we defined a concentration index as 1 divided by the average Euclidean distance from the cluster medoid. High values correspond to increased compactness. Odor groupings were more compact in LIII than in LII (Wilcoxon Signed Rank Test; $p<0.05$).

E. Fraction of neurons that respond to 1 or more odors belonging to a particular class. Stippled lines reflect surrogate distributions where odors are randomly assigned to functional classes. True distributions for each layer were not significantly different from

corresponding control distributions (Wilcoxon Signed Rank Test). Similarly, distributions were not different between layers (Wilcoxon Signed Rank Test).

preference for odors belonging to any particular class (**Figure 3.9 E**). In both layers, most neurons tended to respond only to a fraction of each group.

These results indicate that neural ensembles residing in PCx LIII are better suited for generalizing odorants that are structurally similar while LII ensembles are better-suited for decorrelating similar odorants.

Physicochemical Relationships are Conserved in Piriform Cortex

The striking correspondence between the physicochemical relationships between members in the odor panel and their representations in PCx suggests that Piriform may harbor a relational map of odor space. We therefore constructed distance matrices for odors using physicochemical descriptors as well as odor-evoked activity pooled across both LII and LIII from all three mice (**Figure 3.10 A**). These were significantly correlated (**Figure 3.10 B**) relative to control distributions acquired by bootstrapping chemistry with permuted odor labels (Pearson's r = 0.78; $\text{null distribution mean} = 0.32 \pm 0.05$). **Figure 3.10 C** depicts correspondence of odor pair distances across chemistry and activity spaces.

The observation of strong correspondence between physicochemical properties of odors and their representations in population activity is consistent with the presence of a relational map of odor space in PCx.

Representations of Odor Relationships are Conserved Across Individuals

Topographical maps of sensory information in neocortex are largely consistent across individuals. Cognitive maps in higher-order associative areas reflect differences in individual experience. Given the proposed role for PCx as primarily an associative area, it is

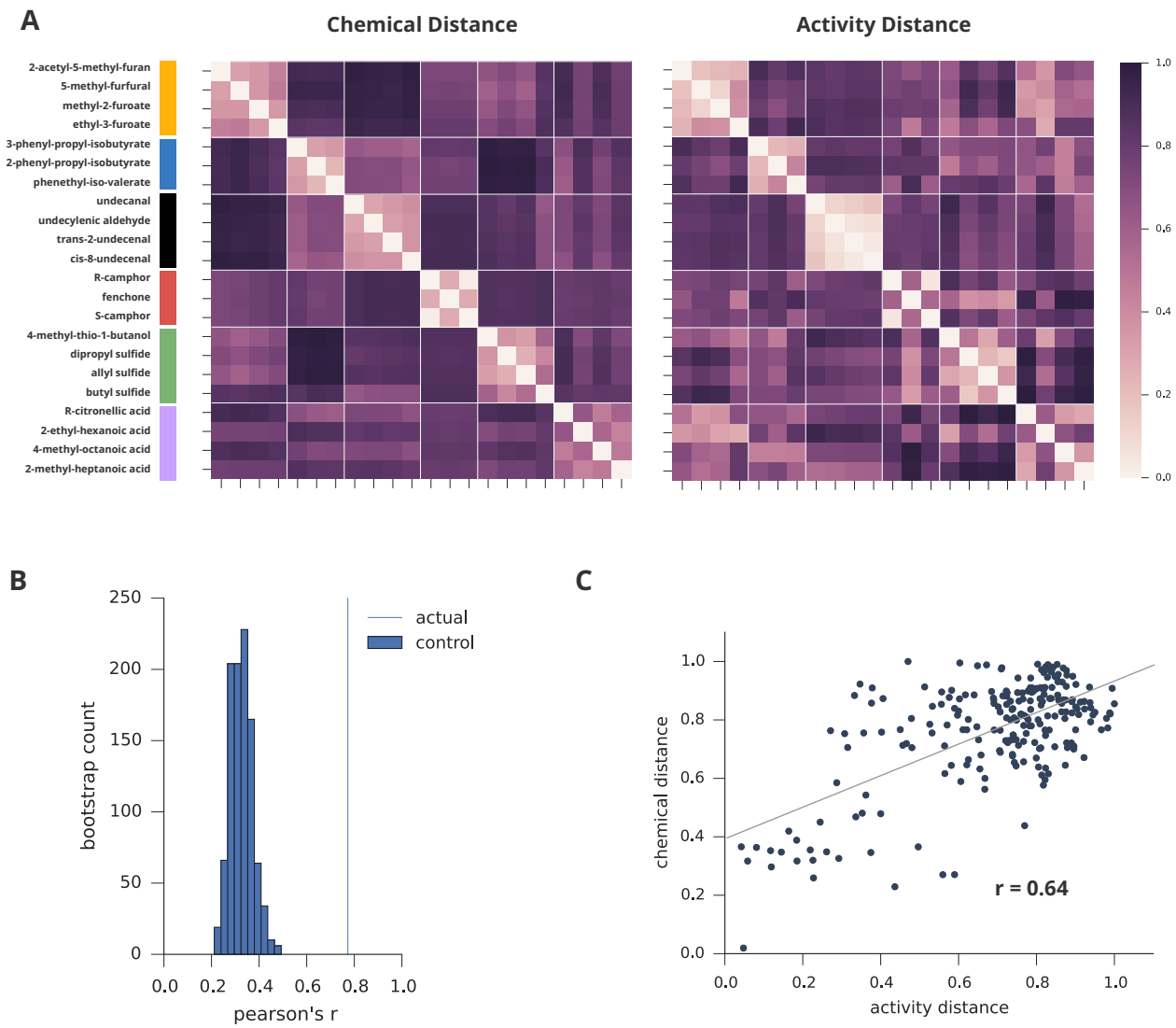

Figure 3.10 Physicochemical Relationships are Conserved in Piriform Cortex

A Distance matrices depicting physicochemical relationships between odorants in the Global odor set (left) and their corresponding relationships in PCx (right). Activity distances were calculated using neurons pooled across both LII and LIII of 3 animals. Distances in chemical space were obtained using the normalized Euclidean distance measure computed for each pair of odors expressed as vectors containing 2270 z-scored descriptor values. Activity

Figure 3.10 (Continued) Physicochemical Relationships are Conserved in Piriform Cortex

distances were obtained by first embedding the pseudopopulation responses in a PCA subspace that capture 50% of the variance. Pairwise relationships were then obtained using normalized Euclidean distance.

B. Pearson's correlation coefficient between Chemical and Activity Distance matrices was 0.78 (vertical line). The control distribution (mean = 0.32 $\pm$ 0.05) represents correlation coefficients obtained by permuting the rows and columns of one of the matrices 1000 times.

C. For each odor-pair, its distance in chemical space is plotted against its corresponding distance in activity space. Regression fit is superimposed. The Pearson correlation coefficient is 0.64. The distribution of coefficients obtained by permutation testing was centered on mean = 0 $\pm$ 0.07.

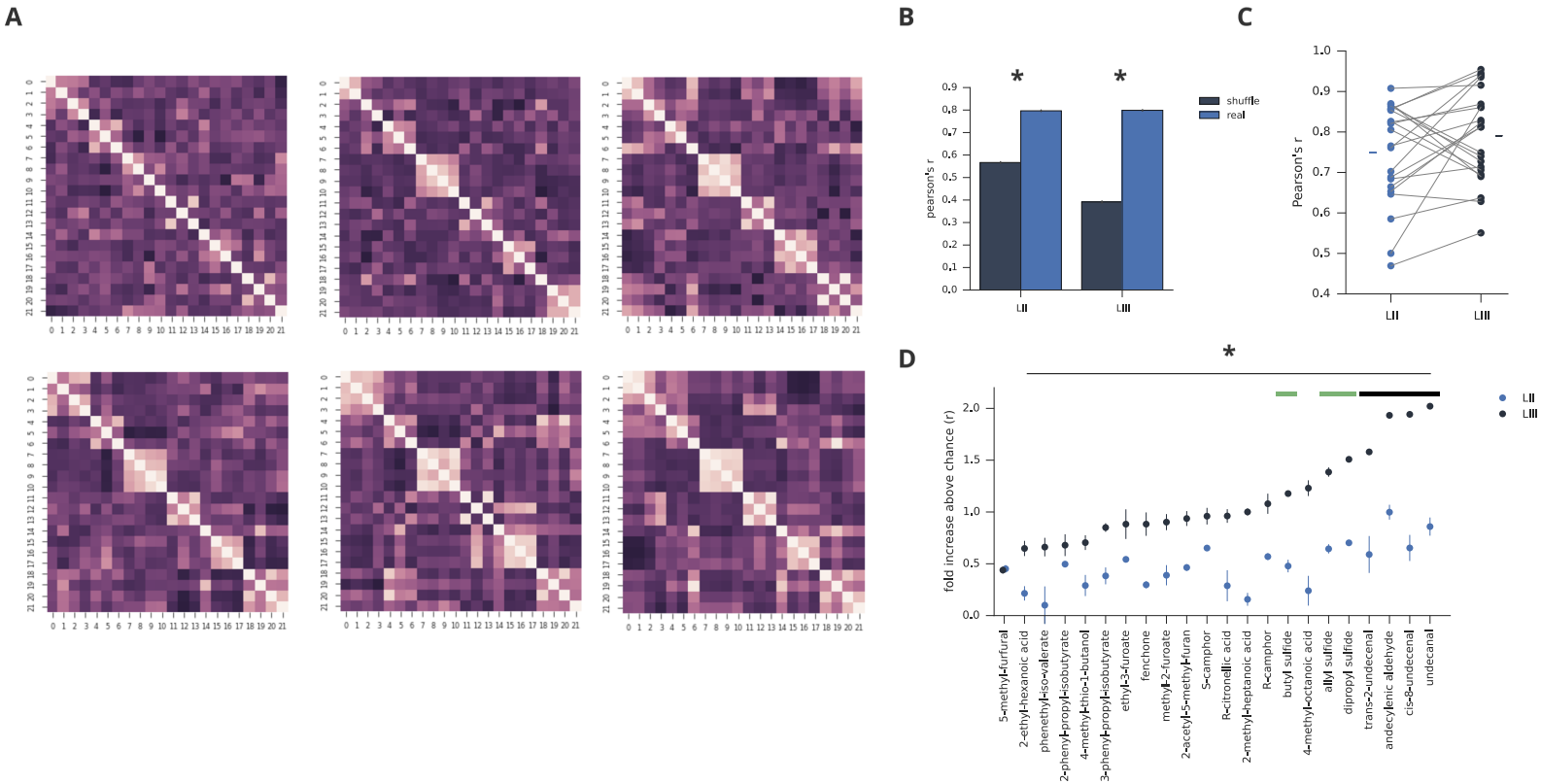

Figure 3.11 Invariance at the Global Scale

A Odor distance matrices constructed from LII (top) and LIII (bottom) odor-evoked activity for 3 separate mice. Odor order is the same as in Figure 3.10. Due to differences in the number of neurons acquired in each condition, activity was first transformed with PCA to explain 50% of the variance for each layer and animal.

.**B**. Average pairwise correlation (Pearson's r) between distance matrices of individual animals indicating conservation of the global structure of odor relationships. For the control condition, odor arrangements in one of the two distance matrices were permuted 1000 times. Error bars indicate 95% confidence intervals of the mean.

Figure 3.11 (Continued) Invariance at the Global Scale

On average, odor arrangements in both LII and LIII were highly conserved across animals, relative to shuffled surrogates (LII mean correlation = 0.74±0.05, LIII = 0.8±0.03; LII shuffle mean correlation = 0.57±0.03, LIII shuffle = 0.39±0.05, Mann Whitney U Test, $p<0.001$). The extent of similarity in odor arrangements between pairs of animals did not differ significantly between layers (Wilcoxon Signed Rank Test).

C. Inter-animal similarity of a single odor's position relative to the other odors in the panel. Here, the Pearson's product moment correlation was computed over pairs of rows corresponding to the same odor from matrices in **A.** Each point represents the average pairwise correlation coefficient for a single odor. Means for each layer are indicated by dashes. On average, an odor's position in the relational space of LIII was slightly, but not significantly, more stable across individual mice than in LII (LIII mean = 0.79±0.1, LII mean = 0.75±0.1, Wilcoxon Signed Rank Test).

D. Same as in **C** except each odor's position relative to the rest of the odor panel is presented as fold-increase above chance correlation. Here, chance correspondence was obtained by shuffling odor relationships in one of 2 distance matrices obtained from separate mice prior to selecting rows corresponding to the odor being compared. Each point represents the mean pairwise increase in Pearson's r. Odors are sorted from least to highest improvement in LIII. Error bars correspond to standard deviation. Overlying bars indicate most reliable classes: sulfurs (green) and aldehydes (black). For each odor

Figure 3.11 (Continued) Invariance at the Global Scale

except 5-methyl-furfural, its relationship to the rest of the panel was significantly more conserved in LIII than in LII (Wilcoxon Signed Rank Test, $p<0.001$).

not clear whether odor similarities and differences are reliably expressed across individuals. Conservation of the odor relationships in neural activity across individuals would suggest that this remapping is an essential feature of centralized odor processing.

To assess the extent of invariance of odor relationships across individuals, we first performed pairwise comparisons between entire distance matrices constructed from odor-evoked activity obtained from single mice (**Figure 3.11 A**). Both LII and LIII exhibited significantly higher correlations on average relative to odor-shuffled controls (**Figure 3.11 B**) (Pearson's r = LII mean = 0.74±0.05 and LIII mean = 0.8±0.03; LII control mean = 0.57 ± 0.03, LIII control mean = 0.39 ± 0.05, Mann Whitney U Test, $p<0.001$).

To assess the extent to which a single odor's position with respect to the rest of the panel was conserved across animals, for each odor, we computed Pearson's r across pairs of rows from distance matrices corresponding to two different animals. In both LII and LIII, correlation values ranged from 0.47 to 0.96 (**Figure 3.11 C**) and were not significantly different between layers (LIII mean = 0.79±0.1, LII mean = 0.75±0.1, Wilcoxon Signed Rank Test). However, when these values were compared against those obtained from odor-shuffled distance matrices, each odor's (except 5-methyl-furfural) position in the relational structure was significantly greater in LIII than in LII (**Figure 3.11 D)** ($p<0.001$, Wilcoxon Signed Rank Test).

The geometry of odor representations, therefore appears to manifest reliably across individuals. Furthermore, the greater invariance of this structure in LIII is consistent with

enhanced stability afforded by populations that operate with a dense code (Spanne & Jörntell, 2015).

Complementary Encoding of Odor Identity and Class

LII and LIII innervate a number of common targets. Relatively decorrelated odor representations in LII and stronger grouping of functional classes in LIII suggests that neurons belonging to each layer may route different aspects of odor information to downstream areas. We therefore took a decoding approach to determine how well odor identity and odor class can be predicted from activity in each layer.

We first trained linear support vector machines to distinguish between all odors in the Global panel using randomly drawn neural ensembles of varying size. Classifiers trained on LII activity outperformed LIII at all ensemble sizes until saturating at 100% accuracy with ensembles composed of around 200 neurons (**Figure 3.12 A**). The greatest gains in accuracy occurred for small ensembles containing 15-30 neurons. Consistent with this observation, individual neurons in LII tended to carry more information about odor identity than in LIII (**Figure 3.12 B**) (LII median = 0.16 vs. LIII median = 0.12, Mann Whitney U Test; $p<0.001$, Cohen's $d = 0.43$).

We then trained decoders to classify odors according to the class to which they belonged. Because distinguishing any two sets of odors should become easier with larger neural ensembles simply due to an increased likelihood of observing differences between high-dimensional activity patterns, for comparison, we trained surrogate decoders after shuffling odor-class assignments. LIII uniformly outperformed LII in odor class assignment

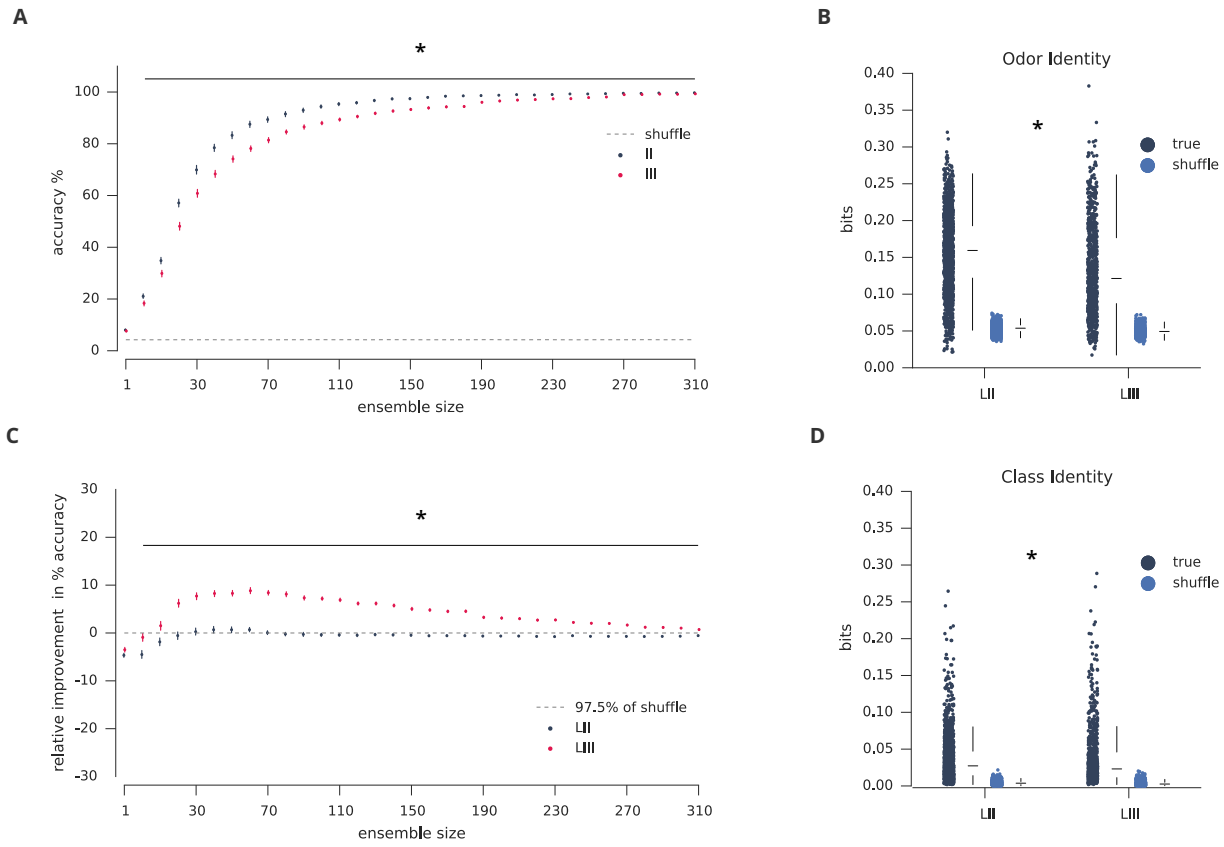

Figure 3.12 Decoding Class and Odor Identity

A Decoding accuracy of linear SVM classifiers trained to identify individual odor presentations. Each dot and associated 95% confidence interval represents the average accuracy of randomly sampled ensembles of the indicated size, obtained from individual animals and subsequently pooled. LII ensembles containing as few as 5 neurons significantly outperform LIII ensembles of similar sizes (Mann Whitney U Test <0.001).

B. Distribution of single neurons' mutual information with respect to odor identity. Odor-response labels were permuted to generate control distributions. Median and

Figure 3.12 (Continued) Decoding Class and Odor Identity

interquartile range of each distribution is indicated with horizontal marker and whiskers. Neurons in LII were considerably more informative (LII median = 0.16 vs. LIII median = 0.12, Mann Whitney U Test; $p<0.001$, Cohen's $d = 0.43$).

C. Same as in **A** but classifiers were trained to assign individual odor presentations to their corresponding class. Each point represents relative improvement in performance above the 97.5^{th} percentile of the chance distribution obtained by randomizing odor-class relationships. LII ensembles containing as few as 5 neurons significantly outperform LIII ensembles of similar sizes (Mann Whitney U Test <0.001).

D. Distribution of single neurons' mutual information with respect to odor class. Odor-class labels were permuted to generate control distributions. Median and interquartile range of each distribution is indicated with horizontal marker and whiskers. In general, individual neurons from both layers provided little information with respect to odor class. Neurons in LII were slightly more informative (LII median = 0.03 vs. LIII median = 0.02, Mann Whitney U Test; $p<0.001$). However, this effect was marginal (Cohen's $d = 0.03$).

even for the smallest ensemble sizes (**Figure 3.12 C**), although significant increases in accuracy were observed for ensembles containing at least 10 neurons.

LIII performance was greatest for ensembles containing roughly 30 neurons and declined in a linear manner thereafter. LII neurons carried slightly more information about odor class than LIII neurons though the magnitude of this difference was negligible (**Figure 3.12 D**) (LII median = 0.03 vs. LIII median = 0.02, Mann Whitney U Test; $p<0.001$, Cohen's $d = 0.03$).

Better classification of odor identity in LII coupled with better class assignment in LIII suggests two types of representational strategies in PCx that could together communicate odor information at multiple scales of similarity.

Interrogating Odor Representations on a Local Scale

Prior studies focusing on the olfactory periphery have benefited from the selection of odor sets consisting of simple molecules, that vary in gradual and intuitive ways.

Straight-chain aliphatic molecules that vary in carbon number have been widely used to demonstrate systematic covariance of responses in olfactory receptor neurons and OB glomeruli across vertebrate (Johnson & Leon, 2007; Meister & Bonhoeffer, 2001; Rubin & Katz, 1999; Uchida, Takahashi, Tanifuji, & Mori, 2000) and invertebrate models (Sachse, Rappert, & Galizia, 1999). In addition, activity patterns induced by these homologous aliphatic series in the rodent OB are precisely arranged and conserved across individuals. (Belluscio & Katz, 2001; Wachowiak, Zochowski, & Cohen, 2000). This conservation is not expected in PCx where odor representations are considered to emerge from the combined

effects of randomly projected OB inputs and strong intrinsic cortical dynamics (Davison, 2011; Franks et al., 2011). Under these conditions, ensemble activity evoked by structurally similar odors is expected to be well-separated and unique to each animal (Stettler & Axel, 2009).

To explore how systematic changes to molecular structure influence PCx odor representations, we designed an odor set that consisted of straight-chain aliphatic molecules containing one of four carbonyl (>C=O) functional groups: ketones, esters, aldehydes, or acids. Carbon tails associated with each functional moiety ranged from 3-8 carbon atoms (**Figure 3.13**). Three mice were used for this experiment.

Two-dimensional PCA embedding of this odor set revealed that carbon atom number (CAN) contributed more weight to PC1 which explained 62% of the variance. Functional group contributed more to PC2 which accounted for 11% of the variance. Collectively, the first 2 PCs accounted for 73% of the variance in the panel—a 12% increase from the Global odor set and a 19% increase from the universal odor set. Consistent with gradual compression in chemical space, the variance of odor-evoked activity decreased accordingly (**Figure 3.14**).

Relationship Between Chemistry and Activity at the Local Scale

Because our Local odor panel varied in both carbon atom number (CAN) and functional group, the precise rearrangement of these molecules in cortical activity could inform which molecular property is the major determinant of central odor representations, and how these representations may differ from those induced in the OB.

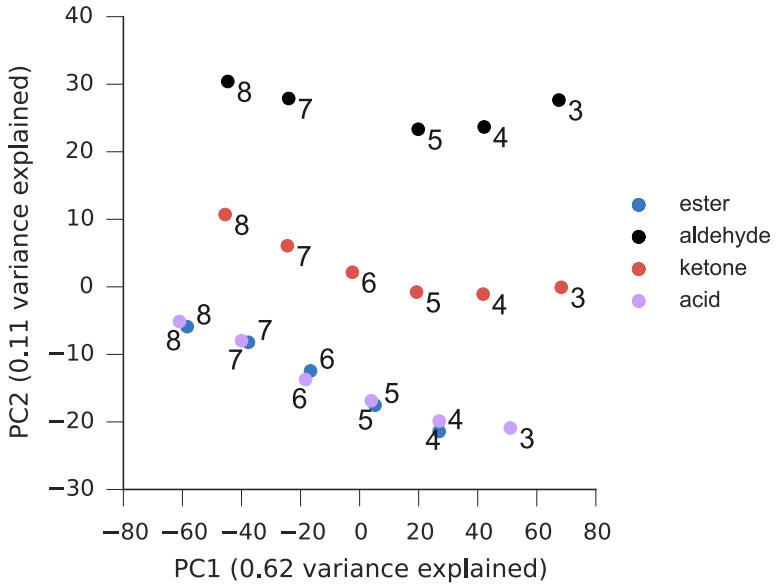

Figure 3.13 Local Odor Set

Projection of 22 odors onto the first 2 principal components of chemical space. Each group of odors contains 5-6 molecules. Numbers indicate size of the carbon backbone.

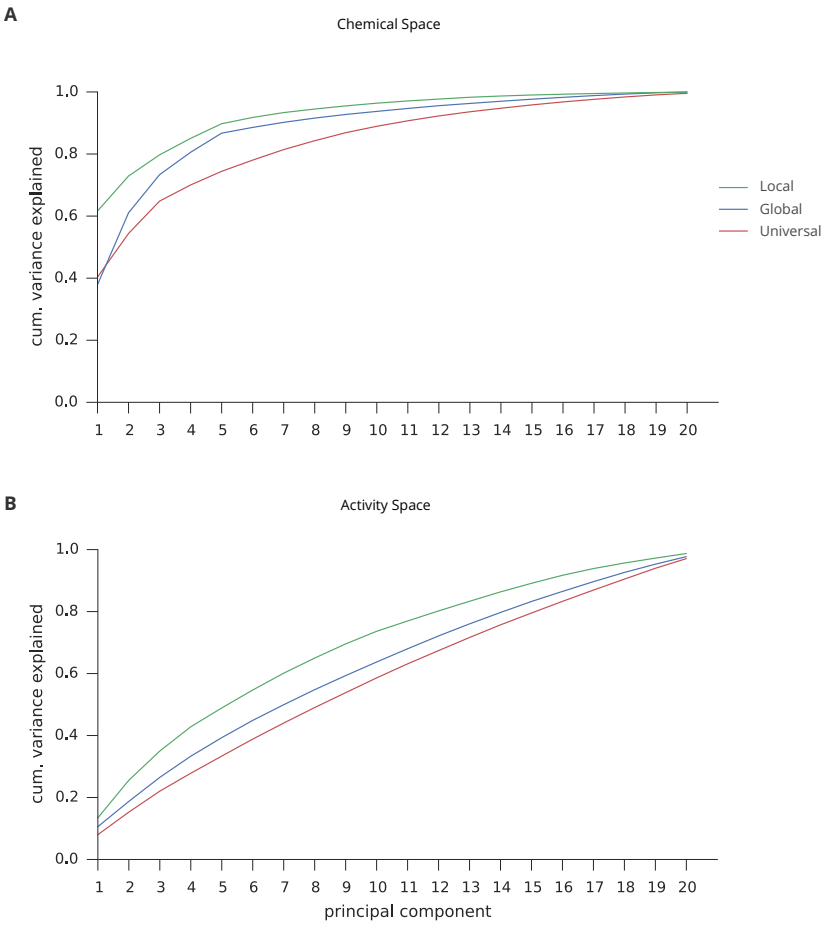

Figure 3.14 Reduction of Variance in Neural Activity with Compression in Odor Space

A. Total variance explained in physicochemical descriptor space plotted against PC number.

B. Identical representation for odor-evoked activity. For this representation activity across both layers and animals was pooled. The first 20 principal components capture 99% of the variance.

We therefore compared similarity arrangements for the Local odor panel against those constructed from odor-evoked activity pooled across layers and animals (**Figure 3.15 A**). There was strong global correspondence between odor relationships and neural activity as compared to a null distribution of correlations constructed by permuting odor arrangements in chemical space **(Figure 3.15 B**) (Pearson's r=0.76, null distribution mean = 0.42 ± 0.04; permutation test). Comparisons for individual odor pairs are presented in **Figure 3.15 C**.

The chemistry distance matrix exhibited strong off-diagonal regularity. High similarity was observed for short-chain as well as long-chain molecules associated with different functional groups as indicated by lighter colors in the matrix. The magnitudes of these similarities across functional group classes was comparable to those of same-class molecules differing in 1 to 3 carbons. Surprisingly, these similarities were substantially attenuated in neural activity. Only esters and ketones remained similar as CAN increased.

To visualize the precise rearrangement of chemistry relationships in each layer, we embedded corresponding response distances obtained from activity pooled across animals in a 2-dimensional subspace using metric multi-dimensional scaling. In chemical space, odors were systematically arranged according to carbon chain length. Aldehydes and ketones appeared to be more similar. This was also the case for esters and acids. In both LII and LIII on the other hand, ketones and esters were much more similar to each other than to the rest of the odor panel (**Figure 3.15 D-F**). Similarity appeared higher for longer chain esters and ketones than their shorter counterparts, especially in LIII. In general,

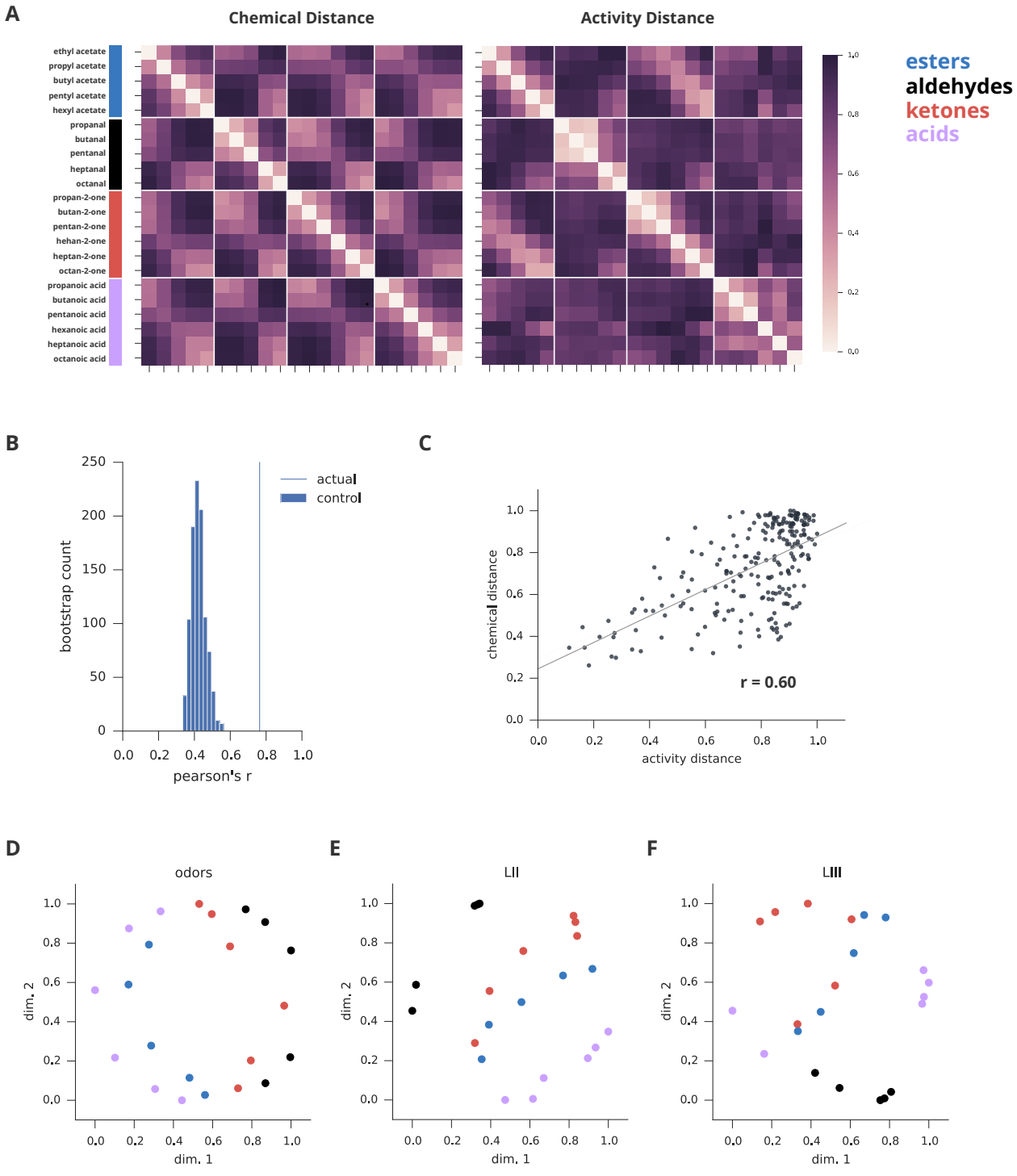

Figure 3.15 Molecular Relationships are Reconfigured at the Local Scale

Figure 3.15 (Continued) Molecular Relationships are Reconfigured at the Local Scale

A Distance matrices depicting physicochemical relationships between molecules in the Local odor set (left) and their corresponding relationships in PCx (right). Both matrices were obtained as described in Figure 3.10 A.

B. Pearson's correlation coefficient between Chemical and Activity Distance matrices was 0.76 (vertical line). The control distribution (mean = 0.42 $\pm$ 0.04) represents correlation coefficients obtained by permuting the rows and columns of one of the matrices 1000 times.

C. For each odor-pair, its distance in chemical space is plotted against its corresponding distance in activity space. Regression fit is superimposed. The Pearson correlation coefficient is 0.6. The distribution of coefficients obtained by permutation testing was centered on mean = 0 $\pm$ 0.07.

D. MDS embedding of odors using physicochemical descriptors. Color indicates functional group.

E. Embedding of odor representations from 3 animals in LII. Short-chain molecules are positioned towards the top of the plot. Aldehyde and acid positions are consistent with chemical arrangements. Esters and ketones are much more closely associated.

F. Same as in **E** but similarity between molecules belonging to different functional classes appears to increase with carbon chain length. Shorter chain molecules lie on the periphery of the circular arrangement (except for the 2 long-chain acids positioned in the bottom left quadrant).

equally good clustering of short-chain and long-chain molecules associated with different functional groups did not hold in LIII; any two groups of shorter-chain molecules appeared to be much better separated, and similarity increased with increasing chain size.

These results indicate that, as observed in the OB, odor representations for homologous series of carbonyl compounds similarly covary with molecular structure. For molecules belonging to a particular functional group, increases in CAN lead to progressive changes in their representations such that separation by more than 3 carbons substantially reduces the similarity of associated ensemble responses. On the other hand, unlike in the olfactory bulb, where glomeruli and mitral cells are often broadly-tuned with respect to short-chain (<5 carbons) carbonyls (Imamura, Mataga, & Mori, 1992; Uchida et al., 2000), in PCx, these groups appear well-separated. This implies that PCx is capable of decorrelating related short-chain odorants according to the unique information carried by their functional groups. The observation that similarity of representations increases with CAN indicates that the contribution of functional group to response specificity is attenuated as molecules become larger.

Invariance Between Animals at the Local Scale

Given the consistency in similarity structure observed across animals with the Global odor set, we similarly asked whether this invariance held for representations of carbonyl series.

To assess the conservation of odor relationships across individuals, we once again constructed distance matrices from odor-evoked ensemble responses obtained from each

layer of individual mice (**Figure 3.16 A**). As observed with the Global odor set, pairwise comparisons of entire distance matrices revealed substantial correlation, on average, relative to odor-shuffled controls (LII mean correlation = 0.81±0.02, LIII mean correlation = 0.85±0.03; LII shuffle = 0.4±0.05, LIII shuffle = 0.31±0.05, Mann Whitney U Test, $p<0.001$) (**Figure 3.16 B**). For both LII and LIII the average similarity was stronger than that observed with the Global odor set.

Comparing any single odor representation's relationships to the rest of the panel revealed a general tendency for stronger conservation in layer III (**Figure 3.16 C**) (LIII mean = 0.85±0.1, LII mean = 0.8±0.1, Wilcoxon Signed Rank Test, $p<0.01$). Consistent with this observation, an odor representation's position in LIII activity space was more stable across animals than in LII relative to correlation values obtained by shuffling distance matrix odor-relationships (**Figure 3.16 D)**.

These results, as well as observations of conserved relational structure using the Global odor panel indicate that odors distributed across multiple scales of volatile space are represented in PCx in a way that's robust to inter-individual differences. Furthermore, the consistent relationship between CAN and OB activity observed across different animals appears to extend to PCx representations as well.

Optimizing Molecular Descriptors for Carbonyl Homologous Series

The 2270 descriptors used in this study differ in the information they carry regarding molecular properties, some of which may not be pertinent for the odors

contained in the homologous series panel. The differences in relational structure between chemical and activity spaces in the Local experiment prompted us to search for better ways of representing molecular structure.

To identify an optimal parsimonious set of descriptors that could explain the representational geometry for the entire set of carbonyl molecules, we performed a type of Monte-Carlo search over descriptor space called Simulated Annealing. Optimal sets were identified by maximizing the similarity of molecular arrangements across chemical and activity spaces.

The optimal number of descriptors was initially chosen with short searches over set sizes ranging from 5 to 100 members (**Figure 3.17 A**). Resulting similarity values ranged from (Pearosn's r) 0.69 to 0.76, suggesting that with this approach, just 5 descriptors are sufficient to improve correspondence between chemistry and activity.

Maximal performance was obtained with descriptor sets containing 35 members, but with multiple random restarts of the algorithm the descriptor occupancy of resulting sets varied substantially, suggesting that despite reaching convergence, the algorithm did not have sufficient time to explore the available space of combinations. We therefore repeated the process by extending the run time until restart reliability saturated. **Figure 3.17 B** depicts selected descriptors' robustness to random restarts. The reliability distribution appeared bimodal. With multiple searches of 35-member sets, 22 descriptors were returned 100 percent of the time. The remaining 13 were chosen only 10% of the time. With smaller or larger set sizes, the fraction of reliably chosen descriptors fell.

Consistent with the substantial redundancy of the entire descriptor space, this variability indicates that in terms of performance, different combinations of descriptors can be used to predict activity equally well.

Molecular relationships constructed using all descriptors that were returned on more than 90% of the runs (**Table 1**) better resembled activity relationships (Pearson's r = 0.84) in several ways (**Figure 3.17 C,D**). Similarity between esters and ketones was retained. For molecules bearing different functional groups, differences between short-chain members was respected, and similarities between their longer-chain versions was conserved.

These results indicate that cortical representations of homologous series of carbonyl molecules occupying a local portion of odor space can be accurately predicted with only 24 physicochemical parameters.

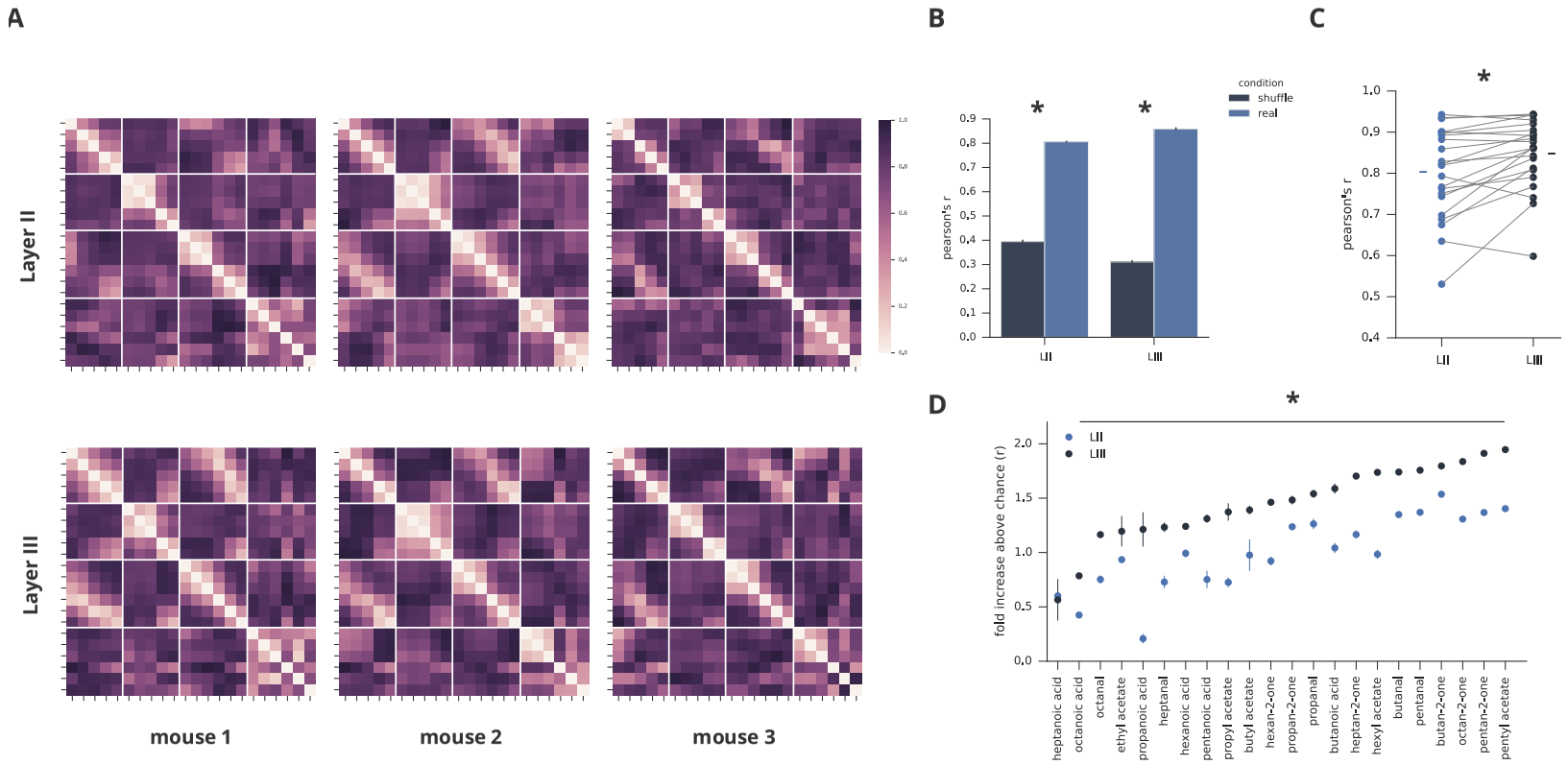

Figure 3.16 Invariance at the Local Scale

A. Odor distance matrices constructed from LII (top) and LIII (bottom) odor-evoked activity for 3 separate mice. Odor order is the same as in Figure 3.15. Due to differences in the number of neurons acquired in each condition, Activity was first transformed with PCA to explain 50% of the variance for each layer and animal.

B. Average pairwise correlation (Pearson's r) between distance matrices of individual animals indicating conservation of the global structure of odor relationships. For the control condition, odor relationships in one of the two distance matrices were permuted 1000 times. Error bars indicate 95% confidence intervals of the mean.

Figure 3.16 (Continued) Invariance at the Local Scale

On average, odor arrangements in both LII and LIII were highly conserved across animals, relative to shuffled surrogates (LII mean correlation = 0.81±0.02, LIII = 0.85±0.03; LII shuffle mean correlation = 0.4±0.05, LIII shuffle = 0.31±0.05, Mann Whitney U Test, $p<0.001$). The extent of similarity in odor arrangements between pairs of animals did not differ significantly between layers (Wilcoxon Signed Rank Test).

C. Inter-animal similarity of a single odor's position relative to the other odors in the panel. Here, the Pearson's product moment correlation was computed over pairs of rows corresponding to the same odor from matrices in **A.** Each point represents the average pairwise correlation coefficient for a single odor. Means for each layer are indicated by dashes. On average, an odor's position in the relational space of LIII was significantly more stable across individual mice than in LII (LIII mean = 0.85±0.1, LII mean = 0.8±0.1, Wilcoxon Signed Rank Test, $p<0.01$).

D. Same as in **C** except each odor's position relative to the rest of the odor panel is presented as fold-increase above chance correlation. Here, chance correspondence was obtained by shuffling odor relationships in one of 2 distance matrices obtained from separate mice prior to selecting rows corresponding to the odor being compared. Each point represents the mean pairwise increase in Pearson's r. Odors are sorted from least to highest improvement in LIII. Error bars correspond to standard deviation. For each

odor except heptanoic acid, its relationship to the rest of the panel was significantly more conserved in LIII than in LII (Wilcoxon Signed Rank Test, $p<0.001$).

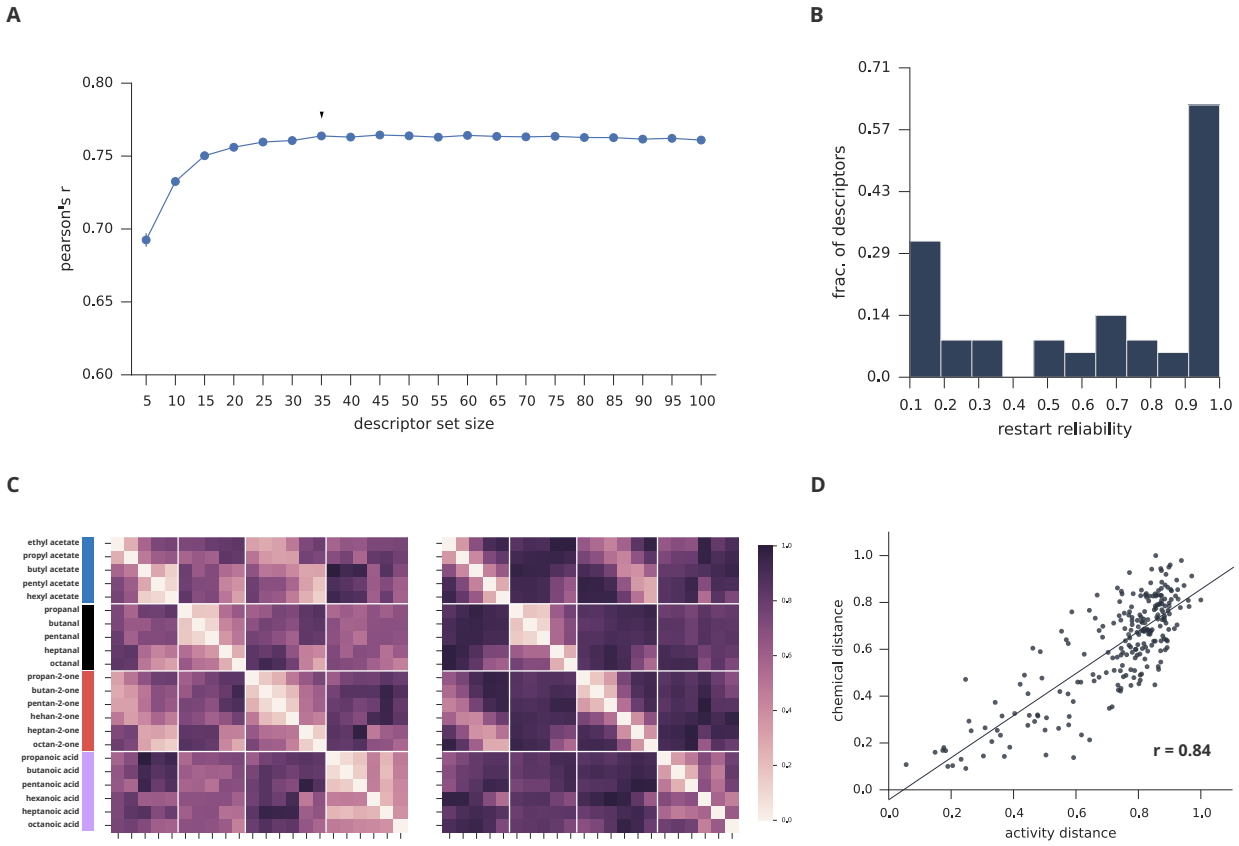

Figure 3.17 Optimization of Physicochemical Descriptors

A. Identification of the smallest number of descriptors with the highest predictive value using simulated annealing. Similarity between chemical and activity distance matrices saturated for descriptor sets containing 35 members (r = 0.76). Maximal similarity when bootstrapping searches with shuffled descriptor values was 0.42.

B. Reliability of selected descriptors upon multiple random restarts of the algorithm. 24 out of 35 descriptors were returned more than 90% of the time.

C. Left: Distance matrices constructed from optimized descriptors. **Right:** Corresponding activity distance matrix, based on responses from all animals and layers.

Figure 3.17 (Continued) Optimization of Physicochemical Descriptors

D. Pairwise odor relationships in chemical and activity spaces. R = 0.84; correlation coefficient obtained using all descriptors is 0.6. Better performance compared to **A** is due to extended annealing times that permit full exploration of descriptor combinations.

Table 1

no.	Molecular Descriptor	Full Name	Descriptor Block
1	MATS3v	Moran autocorrelation of lag 3 weighted by van der Waals volume	2d autocorrelations
2	GATS7m	Geary autocorrelation of lag 7 weighted by mass	2d autocorrelations
3	MATS7e	Moran autocorrelation of lag 7 weighted by Sanderson electronegativity	2d autocorrelations
4	ATSC1s	Centred Broto-Moreau autocorrelation of lag 1 weighted by I-state	2d autocorrelations
5	ATSC1e	Centred Broto-Moreau autocorrelation of lag 1 weighted by Sanderson electronegativity	2d autocorrelations
6	VE1_B(v)	coefficient sum of the last eigenvector (absolute values) from Burden matrix weighted by van der Waals volume	2D matrix-based descriptors
7	Mor08e	signal 08 / weighted by Sanderson electronegativity	3D-MoRSE descriptors
8	Mor27s	signal 27 / weighted by I-state	3D-MoRSE descriptors
9	Mor09p	signal 09 / weighted by polarizability	3D-MoRSE descriptors
10	Mor21m	signal 21 / weighted by mass	3D-MoRSE descriptors
11	Mor28s	signal 28 / weighted by I-state	3D-MoRSE descriptors
12	Mor14s	signal 14 / weighted by I-state	3D-MoRSE descriptors
13	SpMAD_AEA(ri)	spectral mean absolute deviation from augmented edge adjacency mat. weighted by resonance integral	Edge adjacency indices
14	SpMAD_AEA(dm)	spectral mean absolute deviation from augmented edge adjacency mat. weighted by dipole moment	Edge adjacency indices
15	R1m+	R maximal autocorrelation of lag 1 / weighted by mass	GETAWAY descriptors
16	H8u	H autocorrelation of lag 8 / unweighted	GETAWAY descriptors
17	lC2	Information Content index (neighborhood symmetry of 2-order) Radial Distribution Function - 085 / weighted by mass	Information indices
18	RDF100m	Radial Distribution Function - 100 / weighted by mass	RDF descriptors
19	RDF085m	Radial Distribution Function - 085 / weighted by mass	RDF descriptors
20	RDF035m	Radial Distribution Function - 035 / weighted by mass	RDF descriptors
21	E1u	1st component accessibility directional WHIM index / unweighted	WHIM descriptors
22	E1i	1st component accessibility directional WHIM index / weighted by ionization potential	WHIM descriptors
23	L2m	2nd component size directional WHIM index / weighted by mass	WHIM descriptors
24	L2s	2nd component size directional WHIM index / weighted by I-state	WHIM descriptors

Discussion

Olfactory Perception involves a set of neural transformations that convert essential features of the remarkably diverse olfactory environment into neural representations that support adaptive behavior. PCx is considered to be especially important for carrying out a set of general perceptual functions including odor discrimination, generalization, and ultimately long-term storage of diverse odor-associated experiences. Molecular representations in PCx must therefore accommodate these operations, yet their structure at the level of population activity is largely unexplored.

Imaging PCx neural activity in awake mice demonstrates that structural similarities and differences between molecules are—like in the olfactory periphery—maintained in PCx.

Encoding Differences between LII and LIII

Sampling odor-evoked activity across both PCx LII and LIII with a set of diverse odorants reveals several key differences regarding odor encoding across layers. Individual neurons in LII tend to be less sensitive to odor presentation, respond with lower reliability and are selective for a small fraction of the odor set. LIII neurons, on the other hand, are slightly more reliable and tend to have broader response profiles. These results are consistent with previous reports of broader tuning and greater sensitivity of LIII neurons obtained with extracellular recordings in awake mice (Zhan & Luo, 2010).

Consistent with increased sensitivity of individual neurons, odors tended to recruit larger ensembles in LIII than in LII. These effects likely explain the elevated levels of signal

and ensemble correlations observed in deep PCx. Odor encoding in LIII by a shared pool of excitable neurons could result from increased convergence of associative input in deeper PCx, especially in posterior PCx (Hagiwara, Pal, Sato, Wienisch, & Murthy, 2012; Luna & Morozov, 2012) where our recordings were targeted.

Our findings of sparse, selective activation of superficial LII and dense, broadly-tuned activity in deeper LIII is consistent with findings in auditory, somatosensory, and visual (de Kock, Bruno, Spors, & Sakmann, 2007; O'Connor, Peron, Huber, & Svoboda, 2010; Sakata & Harris, 2009) cortex in rodents. The coexistence of these different coding strategies in PCx may serve to both increase information capacity in LII via sparse representations and simultaneously compress these representations for efficient transfer to distal targets in LIII (Coulter, Hillar, & Isley, 2010).

Conservation of Physicochemical Relationships in PCx

Presenting groups of similar odors selected from well-separated portions of odor space as well systematically tiling odor space locally using homologous series of carbonyl molecules revealed that neural activity patterns in both PCx LII and LIII covaried with molecular structure.

Unlike in the OB where molecular similarity is transformed into spatially stereotyped activity, the transformation in PCx involves functional relationships between distributed ensemble activity that likely lack a spatial component. This observation, for the first time, provides empirical evidence that central sensory representations in the olfactory system are organized according to molecular structure. This didn't have to be the case. The current

view in the field is that odor information carried by OB projections is substantially decorrelated by cortical dynamics such that all odors become equally well separated regardless of their structural similarity (Stettler & Axel, 2009). Consistent with this view, discrimination would be optimized but generalization between similar odors would suffer (Spanne & Jörntell, 2015). This compromise is tempered by suggestions that experience-dependent plasticity is essential for establishing perceptual similarity (Haberly, 2001; Wilson & Sullivan, 2011).

Alternatively, and consistent with our results, information regarding molecular similarity is supplied to PCx via correlations in the activity of mitral cells. These correlations are inherited by the cortical population and transformed in a way that preserves the underlying structural similarity between odorants. Providing this information to pools of neurons that differ in coding strategy subsequently permits operations like discrimination and generalization to take place.

Could odor quality be represented in PCx?

Segregation of cortical activity according to molecular structure is sufficient for perceptual operations that involve categorizing or distinguishing odors. One fundamental question is whether the structure of odor-evoked activity also conveys information regarding odor quality. For instance, molecules containing amine and ester moieties are reliably assigned fishy and fruity qualities by human observers (Dravnieks, 1982; Keller & Vosshall, 2016). Given that these odors are well separated in chemical space and should therefore be segregated in PCx activity, classifying new esters and amines should be a

tractable task. However, in the absence of a priori knowledge of the relationships between the activities these odor classes evoke, can a molecule be identified as an ester or an amine based on some feature of neural activity? If piriform cortex is primarily involved in forming stable, unique representations of olfactory experience, this is not required. If, on the other hand, PCx harbors of odor qualities associated with distinct molecular structures, they must be encoded in PCx activity in a way that can be readily interpreted by PCx targets.

This could occur either by means of spatially segregated populations or across functionally distinct groups of neurons. If odor quality involves spatially organized cortical activity, as has been suggested by Gottfried and colleagues based on an fMRI study conducted on human subjects (Howard, Plailly, Grueschow, Haynes, & Gottfried, 2009), it is unlikely to result from anatomically structured projections to PCx, as these appear broadly distributed across the cortical mantle (Ghosh, Larson, Hefzi, Marnoy, & Cutforth, 2011; Miyamichi et al., 2010; Sosulski, Bloom, Cutforth, Axel, & Datta, 2012). Rather, topographic arrangement of odor quality could be inherited from other OB targets like the anterior olfactory nucleus or the cortical amygdala, which are thought to receive spatially biased innervation from the olfactory periphery (Miyamichi et al., 2010; Sosulski et al., 2012); though, the relationship between biased innervation and spatial organization of neural activity remains an open question (Iurilli & Datta, 2017).

In the absence of topographic organization, different odor qualities could be preferentially expressed by discrete groups of neurons with distinct contributions to odor-mediated behaviors. For instance, a class of PCx neurons defined by the expression of the

oxytocin receptor gene has been proposed to influence odor learning in response to salient social cues (Choe, Reed, Benavidez, & Montgomery, 2015). This class of neurons could be preferentially sensitive to urine volatiles. Similarly, PCx subclasses defined by the expression of melanin-concentrating-hormone or neuropeptide-Y receptor genes, implicated in energy homeostasis, could be preferentially tuned to food odors. In this case, assignment of distinct odor qualities to specific classes of neurons would likely have to emerge through experience, and their detection would require monitoring activity across genetically tagged neural populations.

Alternatively, if molecular structure is encoded by a homogeneous neural pool, specific odor qualities could be represented by differences in the temporal patterning of activity or variations in population firing rate. These differences could reflect distinct molecular mechanisms associated with ligand-receptor interactions. For example, the exceptionally low perceptual thresholds for malodorous sulfur containing odors (Laska, Bautista, Höfelmann, Sterlemann, & Salazar, 2007) have been related to unique detection mechanisms involving selective and high-affinity ligand-receptor interactions via metal ion intermediates in the binding cavity (Noe et al., 2017; Wang, Luthey-Schulten, & Suslick, 2003). In general, differences in molecular size, atomic arrangement, and composition all affect molecular access to the aqueous environment of the nasal epithelium and subsequently, binding affinity across the receptor array. This could ultimately influence the size of recruited ensembles in PCx, as well as the synchrony, latency, and amplitude of responses of constituent neurons. All of these properties could potentially be read out by

downstream targets of PCx to support stable representations of odor qualities capable of eliciting innate, ethologically relevant behaviors.

General Conclusions

A map is an expression of fixed, reliable relationships among a set of entities designed to facilitate prediction of higher-order interactions between them. For example, on a geographical map, distance is a reliable metric that allows one to predict how long it would take to travel between two locales. The fact that this distance does not change from day to day and that its' representation remains constant allows the planning of routes and itineraries that lead to more efficient behavior. Maps based on unreliable metrics quickly lose their utility.

Nervous systems similarly harbor maps of the external environment to facilitate adaptive behavior. Because most experience requires engagement in 3d space, these maps are often designed to accommodate ordered spatial relationships in the outside world. The brainstem auditory localization map of barn owls, for instance, is spatially optimized for temporal triangulation of auditory sources (Konishi, 1971).

Systematic arrangements of sensory information in neural circuits has also been suggested to emerge from metabolic constraints on nervous system packaging (Chklovskii & Koulakov, 2000; 2004; Koulakov & Chklovskii, 2001).

From an experimental point of view, topographic arrangement of sensory information in cortex has simplified attempts to characterize computations performed by neural circuits (Nassi & Callaway, 2009) and becomes especially useful in the absence of a

priori knowledge of what relationships in the outside world are selectively represented in the brain (Hubel & WIESEL, 1962). In the absence of topographic organization, this information must be gleaned exclusively from measuring functional relationships between sensory-evoked patterns of activity.

Despite considerable effort, topographic remapping of odors in central olfactory areas has yet to be identified in any organism, but see (Nikonov & Finger, 2005). This is likely because olfaction is not primarily a “spatial sense,” and odor processing beyond the olfactory bulb may therefore not be bound by the same energy-minimizing physiological constraints imposed on visual, somatosensory, or auditory cortical circuits.

This ultimately means that understanding how the brain transforms the structure inherent in the volatile world to neural correlates of perception and behavior will likely benefit from top-down experimental strategies where ordered relationships in population activity are subsequently linked to structural properties of odorous molecules.

References

Averbeck, B. B., Latham, P. E., & Pouget, A. (2006). Neural correlations, population coding and computation. *Nature Reviews Neuroscience*, *7*(5), 358–366. http://doi.org/10.1038/nrn1888

Belluscio, L., & Katz, L. C. (2001). Symmetry, Stereotypy, and Topography of Odorant Representations in Mouse Olfactory Bulbs. *The Journal of Neuroscience*, *21*(6), 2113–2122. http://doi.org/10.1016/0165-0173(94)90007-8

Chklovskii, D. B., & Koulakov, A. A. (2000). A wire length minimization approach to ocular dominance patterns in mammalian visual cortex. *Physica a: Statistical Mechanics and Its Applications*, *284*(1-4), 318–334. http://doi.org/10.1016/S0378-4371(00)00219-3

Chklovskii, D. B., & Koulakov, A. A. (2004). MAPS IN THE BRAIN: What Can We Learn from Them? *Dx.Doi.org.Ezp-Prod1.Hul.Harvard.Edu*, *27*(1), 369–392. http://doi.org/10.1146/annurev.neuro.27.070203.144226

Choe, H. K., Reed, M. D., Benavidez, N., & Montgomery, D. (2015). Oxytocin mediates entrainment of sensory stimuli to social cues of opposing valence. *Neuron*. http://doi.org/10.1016/j.neuron.2015.06.022

Cohen, J. (1992). Statistical power analysis. *Current Directions in Psychological Science*.

Coulter, W. K., Hillar, C. J., & Isley, G. (2010). Adaptive compressed sensing—a new class of self-organizing coding models for neuroscience. *Acoustics Speech and …*. http://doi.org/10.1109/ICASSP.2010.5495209

Davison, I. (2011). Neural circuit mechanisms for pattern detection and feature combination in olfactory cortex. *Neuron*.

de Kock, C. P. J., Bruno, R. M., Spors, H., & Sakmann, B. (2007). Layer- and cell-type-specific suprathreshold stimulus representation in rat primary somatosensory cortex. *The Journal of Physiology*, *581*(1), 139–154. http://doi.org/10.1113/jphysiol.2006.124321

Dravnieks, A. (1982). Odor quality: semantically generated multidimensional profiles are stable. *Science*.

Franks, K. M., Russo, M. J., Sosulski, D. L., Mulligan, A. A., Siegelbaum, S. A., & Axel, R. (2011). Recurrent Circuitry Dynamically Shapes the Activation of Piriform Cortex. *Neuron*, *72*(1), 49–56. http://doi.org/10.1016/j.neuron.2011.08.020

Ghosh, S., Larson, S. D., Hefzi, H., Marnoy, Z., & Cutforth, T. (2011). Sensory maps in the olfactory cortex defined by long-range viral tracing of single neurons. *Nature*.

Haberly, L. B. (2001). Parallel-distributed Processing in Olfactory Cortex: New Insights from Morphological and Physiological Analysis of Neuronal Circuitry. *Chemical Senses*, *26*(5), 551–576. http://doi.org/10.1093/chemse/26.5.551

Hagiwara, A., Pal, S. K., Sato, T. F., Wienisch, M., & Murthy, V. N. (2012). Optophysiological analysis of associational circuits in the olfactory cortex. *Frontiers in Neural Circuits*, *6*, 18. http://doi.org/10.3389/fncir.2012.00018

Howard, J. D., Plailly, J., Grueschow, M., Haynes, J.-D., & Gottfried, J. A. (2009). Odor quality coding and categorization in human posterior piriform cortex. *Nature Neuroscience*, *12*(7), 932–938. http://doi.org/10.1038/nn.2324

Hubel, D. H., & WIESEL, T. N. (1962). Receptive fields, binocular interaction and functional architecture in the cat's visual cortex. *The Journal of Physiology*, *160*, 106–154.

Iurilli, G., & Datta, S. R. (2017). Population Coding in an Innately Relevant Olfactory Area. *Neuron*, *93*(5), 1180–1197.e7. http://doi.org/10.1016/j.neuron.2017.02.010

Imamura, K., Mataga, N., & Mori, K. (1992). Coding of odor molecules by mitral/tufted cells in rabbit olfactory bulb. I. Aliphatic compounds. *Journal of Neurophysiology*.

Johnson, B. A., & Leon, M. (2007). Chemotopic odorant coding in a mammalian olfactory system. *The Journal of Comparative Neurology*, *503*(1), 1–34. http://doi.org/10.1002/cne.21396

Keller, A., & Vosshall, L. B. (2016). Olfactory perception of chemically diverse molecules. *BMC Neuroscience*, 1–17. http://doi.org/10.1186/s12868-016-0287-2

Konishi, M. (1971). Sound Localization in the Barn Owl. *The Journal of the Acoustical Society of America*.

Koulakov, A. A., & Chklovskii, D. B. (2001). Orientation preference patterns in mammalian visual cortex: a wire length minimization approach. *Neuron*.

Laska, M., Bautista, R. M. R., Höfelmann, D., Sterlemann, V., & Salazar, L. T. H. (2007). Olfactory sensitivity for putrefaction-associated thiols and indols in three species of non-human primate. *Journal of Experimental Biology*, *210*(23), 4169–4178. http://doi.org/10.1242/jeb.012237

Luna, V. M., & Morozov, A. (2012). Input-specific excitation of olfactory cortex microcircuits. *Frontiers in Neural Circuits*. http://doi.org/10.3389/fncir.2012.00069

Meister, M., & Bonhoeffer, T. (2001). Tuning and topography in an odor map on the rat olfactory bulb. *The Journal of Neuroscience : the Official Journal of the Society for Neuroscience*, *21*(4), 1351–1360.

Miyamichi, K., Amat, F., Moussavi, F., Wang, C., Wickersham, I., Wall, N. R., et al. (2010). Cortical representations of olfactory input by trans-synaptic tracing. *Nature*. http://doi.org/doi:10.1038/nature09714

Nassi, J. J., & Callaway, E. M. (2009). Parallel processing strategies of the primate visual system. *Nature Reviews Neuroscience*, *10*(5), 360–372. http://doi.org/10.1038/nrn2619

Nikonov, A., & Finger, T. (2005). Beyond the olfactory bulb: an odotopic map in the forebrain. *Proceedings of the …*.

Noe, F., Polster, J., Geithe, C., Kotthoff, M., Schieberle, P., & Krautwurst, D. (2017). OR2M3: A Highly Specific and Narrowly Tuned Human Odorant Receptor for the Sensitive Detection of Onion Key Food Odorant 3-Mercapto-2-methylpentan-1-ol. *Chemical Senses*, *42*(3), 195–210. http://doi.org/10.1093/chemse/bjw118

O'Connor, D. H., Peron, S. P., Huber, D., & Svoboda, K. (2010). Neural activity in barrel cortex underlying vibrissa-based object localization in mice. *Neuron*. http://doi.org/10.1016/j.neuron.2010.08.026

Pachitariu, M., Stringer, C., Dipoppa, M., & Schröder, S. (2017). Suite2p: beyond 10,000 neurons with standard two-photon microscopy. *BioRxiv*. http://doi.org/10.1101/061507

Rubin, B. D., & Katz, L. C. (1999). Optical imaging of odorant representations in the mammalian olfactory bulb. *Neuron*, *23*(3), 499–511.

Sachse, S., Rappert, A., & Galizia, C. G. (1999). The spatial representation of chemical structures in the antennal lobe of honeybees: steps towards the olfactory code. *European Journal of …*.

Sakata, S., & Harris, K. D. (2009). Laminar Structure of Spontaneous and Sensory-Evoked Population Activity in Auditory Cortex. *Neuron*, *64*(3), 404–418. http://doi.org/10.1016/j.neuron.2009.09.020

Sosulski, D. L., Bloom, M. L., Cutforth, T., Axel, R., & Datta, S. R. (2012). Distinct representations of olfactory information in different cortical centres. *Nature*, *472*(7342), 213–216. http://doi.org/10.1038/nature09868

Spanne, A., & Jörntell, H. (2015). Questioning the role of sparse coding in the brain. *Trends in Neurosciences*, *38*(7), 417–427. http://doi.org/10.1016/j.tins.2015.05.005

Stettler, D. D., & Axel, R. (2009). Representations of Odor in the Piriform Cortex. *Neuron*, *63*(6), 854–864. http://doi.org/10.1016/j.neuron.2009.09.005

Uchida, N., Takahashi, Y. K., Tanifuji, M., & Mori, K. (2000). Odor maps in the mammalian olfactory bulb: domain organization and odorant structural features. *Nature Neuroscience*, *3*(10), 1035–1043. http://doi.org/10.1038/79857

Vinje, W. E., & Gallant, J. L. (2000). Sparse coding and decorrelation in primary visual cortex during natural vision. *Science*.

Wachowiak, M., Zochowski, M., & Cohen, L. B. (2000). The spatial representation of odors by olfactory receptor neuron input to the olfactory bulb is concentration invariant. *The Biological …*. http://doi.org/10.2307/1542876

Wang, J., Luthey-Schulten, Z. A., & Suslick, K. S. (2003). Is the olfactory receptor a metalloprotein? *Proceedings of the National Academy of Sciences of the United States of America*, *100*(6), 3035–3039. http://doi.org/10.1073/pnas.262792899

Willmore, B., & Tolhurst, D. J. (2001). Characterizing the sparseness of neural codes. *Network (Bristol, England)*, *12*(3), 255–270.

Wilson, D. A., & Sullivan, R. M. (2011). Cortical Processing of Odor Objects. *Neuron*, *72*(4), 506–519. http://doi.org/10.1016/j.neuron.2011.10.027

Zhan, C., & Luo, M. (2010). Diverse patterns of odor representation by neurons in the anterior piriform cortex of awake mice. *Journal of Neuroscience*, *30*(49), 16662–16672. http://doi.org/10.1523/JNEUROSCI.4400-10.2010